Study of serpentine acceleration in zero-chromatic FFAG accelerators

Emi Yamakawa

Abstract

A new type of fixed rf frequency acceleration scheme so-called serpentine acceleration is applied in scaling FFAG to realize rapid beam acceleration and produce high-intensity beams. With serpentine acceleration schemes, particles are accelerated in the serpentine channel which is around both stationary buckets below and above the transition energy.

To study a fixed rf frequency acceleration scheme in longitudinal phase space, longitudinal hamiltonian in scaling FFAG with fixed rf frequency is derived analytically as follows

$$H(E, \phi; \Theta) = h \left[\frac{1}{\alpha + 1} \frac{(E^2 - m^2)^{\frac{\alpha+1}{2}}}{E_s (E_s^2 - m^2)^{\frac{\alpha-1}{2}}} - E \right] + \frac{eV_0}{2\pi} \cos \phi,$$

with canonically conjugated variables phase ϕ and energy E. The parameter h is the harmonic number, α is the momentum compaction factor, V_0 is the peak rf voltage, E_s is the stationary energy and m is the rest mass. With this longitudinal hamiltonian, features of serpentine acceleration scheme is investigated analytically.

Lowest limit of rf voltage called minimum rf voltage to make a serpentine channel has been derived from longitudinal hamiltonian. Besides, energy range of serpentine channel from bottom to top have been evaluated with rf voltage. Phase acceptance of serpentine channel has been also examined with rf voltage. Since sinusoidal rf voltage wave is used in serpentine acceleration, energy spread at extraction becomes large with wide range of injected phase. To avoid large energy spread at extraction, applying a higher-order harmonics of square rf voltage wave has been proposed. Longitudinal hamiltonian with fixed rf frequency and square rf voltage wave has been derived analytically, and longitudinal beam dynamics has been studied. Estimation of effect of applying a higher-order harmonics of square rf voltage wave also has been evaluated.

To clarify and demonstrate a serpentine acceleration in scaling FFAG, beam experiments have been carried out with electron scaling FFAG machine. First, beam acceleration with serpentine channel has been demonstrated. Then phase acceptance of serpentine acceleration has been measured with rf voltage and compared with longitudinal calculation result. Application of proton driver for ADS with serpentine acceleration is finally proposed.

Acknowledgments

I would like to express my sincere appreciation to my supervisor, Professor Yoshiharu Mori. He gave me not only the chance to study accelerator physics but also a lot of helpful comments and unique ideas.

I am deeply grateful to Prof. Izumi Sakai, Dr. Yoshihiro Ishi, Dr. Tomonori Uesugi, Dr. Kota Okabe, Dr. Yasutoshi Kuriyama, Dr. Qin Bin, Dr. Thomas Plance, and Dr. J.-B Lagrange for their continuous and warm support. They gave me a lot of helpful and useful advice and suggestions.

And I also wish to express my gratitude to Dr.Shoroku Ohnuma. He gave me many useful comments and cheered me up.

I gratefully acknowledge Dr. Yoshimasa Yuasa and all the people of NHVC to carry out experiments.

I would like to thank Yuka Ono, Keiko Fujiwara, Chika Nakamura, Fujie Takashima and Mayumi Mikura. All of them helped me for my graduate school life.

I wish to express my warm and sincere gratitude to all the member of the research team, who all helped me during this study: Hideki Imazu, Masashi Takashima, Yoshihiro Takahoko, Ryotarou Nakano, Yusuke Niwa, Tomoya Minamikawa, Yasuhiro Ito, and Mao Takabatake.

Last but not least, I would like to express my deepest appreciation to my parents, my sister, my grand parents and my friends. I could not complete my graduate course without their all kindly support.

Contents

CHAPTER 1

Introduction

1.1 Background

Electron accelerators are used in many fields in these years. One of them is the medical industry, with the sterilization of medical instruments by electron beams. Another one is food industry. Food is exposed to electron beams to kill insects and avoid germination. Other applications for using electron beams are cable processing and X-ray portal scanners. In these applications, it is desired to irradiate materials at one time. Thus, providing high-intensity electron beam is required for theses accelerators.

In the academic field, accelerators have been developed in physics so far. In this field, muon facilities are good candidates for the next generation of high energy physics experiments. Muon colliders and neutrino factories [1, 2] are indeed seriously considered these days. In such experiments, high-energy and high-intensity muon beams are required. Besides, due to the short muon lifetime ($\backsim 2.2\mu s$), very fast acceleration ($\backsim \mu s$) is needed to accelerate beams within a lifetime.

Not only particle physics but also nuclear engineering shows a great interest in accelerators in recent years. In this field, disposal of Minor actinides (MA) and Long-lived fission products (LLFP) radioactive waste is an important issue. Accelerator Driven System (ADS) [3] is one of the ways to handle this problem, and is attractive all over the world. The ADS consists of a subcritical reactor that is driven by an external neutron source produced by a high-power proton beam hitting a heavy metal material and producing neutrons by spallation. Furthermore, it can utilize both Uranium and Thorium as a nuclear fuel and produce energy without producing long-lived radioactive wastes [4]. To generate enough spallation neutrons, the accelerator for ADS is required to deliver a high-energy and high-intensity up to several tens of MW proton beam. When high-intensity beam is obtained,

betatron tune shifts caused by space charge effect [5] can become a problem. Rapid acceleration is one solution to overcome this issue.

In consequence, accelerators need to achieve the rapid beam acceleration. Furthermore, producing high-power beam is also desired.

1.2   Requirements for accelerators

In order to realize rapid beam acceleration and producing high-power beams, necessary conditions for accelerators are considered as follows.

It is not suitable to vary the field of bending magnets for rapid beam acceleration. For ordinary synchrotrons, magnetic field varies in time with beam energy to keep the same orbit. In ordinal case in synchrotrons, varying frequency of magnetic field is about 1 Hz. In the 3 GeV rapid-cycle proton synchrotron (RCS) in Japan Proton Accelerator Research Complex (J-PARC) [6], bending magnets are driven by the rapid-cycle system with 25 Hz. However, even with rapid-cycle system, repetition time is larger than the muon decay period. Furthermore, magnetic field with rapid-cycles (> 25 Hz) creates eddy current which flows along the metallic elements of the magnet including beam chamber, causing beam loss [7]. From these considerations, bending magnet with static field is suitable for rapid beam acceleration.

Another issue is the production of high average current beams. For this requirement, two approaches are considered. One way is to increase the amount of injection particles per bunch. In this case, however, the number of injected particles are limited by the space charge effect. The other method is using a rf cavity with fixed rf frequency. Since beam acceleration with continuous wave (c.w.) mode can be carried out, high-intensity beams with rapid-repetition rate can be generated, free from space charge effect. Fixed rf frequency acceleration scheme is adapted in linear accelerators and cyclotrons in general.

To accelerate secondary particles such as muons, large dynamic aperture is secured for the acceleration with large emittance beams stably. Thus, strong focusing [8] needs to be applied in the machine.

From the consideration above, to obtain the high-intensity and rapid-acceleration stably, accelerators are necessarily satisfied with the following conditions: (i) static guide field, (ii) fixed rf frequency and (iii) strong focus-

ing principle.

1.2.1   Candidates of accelerators

Candidates of the accelerators fulfilling these three requirements to obtain
a high-intensity and rapid-acceleration system are linear accelerators so far.
Linear accelerators have been considered for muon acceleration in neutrino
factory and for generation of high-intensity proton beam for ADS [9]. How-
ever, since a beam passes through once a cavity in linear accelerators, number
of cavities in a line are increased according to the final beam energy. Due to
this issue, the area for installation of many rf cavities is secured. Furthermore
their cost make practical realization difficult.

Other possible candidates for accelerators satisfied with the requirements
are circular accelerators. Representative examples in circular accelerators
are classical cyclotrons and synchrotrons. Classical cyclotrons are operated
with a static magnetic field and a fixed rf frequency. However, the bending
magnet in cyclotron is based on weak focusing. On the other hand, in classical
synchrotrons, they use strong focusing principle. However, magnetic field and
rf frequency vary according to beam energy. Therefore, classical cyclotrons
and synchrotrons do not satisfy all the requirements.

In the late 1950s, a new type of circular accelerator, Fixed Field Alter-
nating Gradient (FFAG) accelerator, was innovated [10, 11, 12]. The guiding
magnetic field in FFAG accelerator is static as cyclotrons. Strong focusing
is also realized, alternating a focusing and defocusing element. Fixed rf fre-
quency can be also achieved in beam acceleration [13]. FFAG accelerator
thus satisfies the three necessary conditions to realize a high-intensity and
rapid-acceleration scheme.

1.3   FFAG accelerator

FFAG accelerator was originally proposed by Symon, Kolomenskii and
Okawa independently in the late 1950s [10, 11, 12]. At that time, three pro-
totype of electron FFAG accelerators [14, 15, 16] were built at Midwestern
Universities Research Association (MURA) [17]. However practical FFAG
rings had not been realized for about 40 years. One reason was that mag-
net size becomes big compared to synchrotrons. Furthermore, it was hard

to construct the magnetic field with sufficient accuracy. The other problem was the construction of the rf cavity which have a large aperture to cover the large orbit shifts. High gradient rf field and broadband cavity were also necessary in order to utilize rapid acceleration in FFAG accelerator.

These problems were resolved by advancement of technology in recent years. The complicated magnet design can be realized by three-dimensional magnetic field calculation tools. A broadband and high gradient rf cavity have been also achievable with Magnetic Alloy (MA) cores [18] at KEK. In 2000, the world first proton FFAG accelerator, so called POP-FFAG [19], was demonstrated at KEK. From this success, the rapid acceleration scheme of proton beam with a repetition rate of 1 kHz was achieved in FFAG accelerator.

FFAG accelerators are categorized in terms of magnetic field; non-scaling FFAG and scaling FFAG. The scaling FFAG ring is composed of non-linear variation of the magnetic field strength with radius. This magnetic field variation brings a constant betatron tune with particle momentum, called zero chromaticity. For this reason, scaling FFAG is called zero-chromatic FFAG. On the other hand, in non-scaling FFAGs, a linear variation of magnetic field is employed. Orbits at different momenta have different shapes in this machine, resulting in large betatron tune changes during beam acceleration. Therefore, very fast acceleration must be achieved to avoid the beam loss by resonance crossing during beam acceleration.

Both type of FFAG accelerators are built and used for many applications. In scaling FFAGs, the world first ADS using spallation neutrons generated by proton beam started at Kyoto University Research Reactor Institute (KURRI) in March 2009 [20, 21]. The PRISM FFAG ring composed of scaling FFAG is developed to produce pure and quasi mono-energetic muon beams with phase rotation [22, 23, 24, 25]. It is constructed at Osaka University. Moreover the production of intense source of secondary particles from proton beams has been developed with the energy recovering internal target (ERIT) scaling FFAG schemes [26, 27]. On the other hand, in non-scaling FFAG, the world first electron prototype, called EMMA (Electron Model for Many Applications), has been constructed at the STFC Daresbury Laboratory in the United Kingdom.

1.4 Fixed rf acceleration scheme in FFAG accelerators

Various methods of beam acceleration using rf cavities have been proposed for FFAG accelerators. The ordinary way is realized with frequency modulation of the rf system. With this scheme, injected beam is captured in an rf bucket. Since the synchronous energy is changed with modulation of the rf frequency, the acceleration repetition rate is determined by the changing speed of rf frequency. However, if rf voltage is not large enough, beam cannot gain the energy to be captured by the rf bucket, causing beam loss. Therefore, beam intensity is limited by the rf systems. Another scheme is the stationary bucket acceleration where rf frequency is fixed. Once the rf frequency is fixed, two stationary buckets below and above the transition energy are also fixed respectively. In a stationary bucket acceleration scheme, an injected beam is accelerated in an rf bucket. Since c.w. operation becomes possible, a larger current beam can be obtained rather than sweeping rf frequency system.

In scaling FFAG, the stationary bucket acceleration scheme has been studied so far [28, 29]. In this scheme, since beam can be accelerated only in a stationary bucket, the total acceleration energy gain from injection to extraction is limited by the bucket height. In order to increase the bucket height, a huge rf voltage should be applied. Another way to increase the bucket height is that slippage factor should be chosen around zero. It means the beam is accelerated near the transition energy. Moreover, relativistic energy beams are suitable for increasing the rf bucket height.

On the other hand in non-scaling FFAG, since shape of closed orbits do not scale with particle energy, momentum compaction factor is not constant. It may cause orbit excursion huge. With the appropriate selection of parameters such as magnet configuration, a parabolic variation in orbit length with energy can be created. At the minimum of the parabola, the momentum compaction factor approaches zero and remains very small. It means the orbit shifts with energy variations can be much smaller, allowing much more compact magnets than in other fixed field accelerators. Furthermore, for relativistic particles with the parabolic variation in orbit length, time of flight is also approximately parabolic. Then the decreased variation in orbital period allows to operate a fixed rf frequency acceleration with an

appropriate selection of rf frequency and a high enough rf voltage. This new type of fixed rf frequency acceleration scheme is called serpentine acceleration [30, 31, 32, 33]. In serpentine acceleration, injected beams are accelerated around both stationary buckets. With this acceleration scheme, total energy gain from injection to extraction is larger than a stationary bucket acceleration. Furthermore rapid-acceleration can be achieved, since particles are accelerated near the rf phase 90 degrees.

1.5   Purpose of the study

In elementary particle physics, lepton flavor violation of charged leptons has been attractive subject to find a new physics [23, 24]. For this experiment, low energy muon beam less than 100 MeV is desired. In this case, muon particles cannot be accelerated within lifetime without a rapid-acceleration scheme in non-relativistic energy region. In other fields, around 1 GeV proton beam with c.w. modes are required for ADS in nuclear engineering. For these requirements to accelerators, a fixed rf frequency acceleration scheme is secured in non-relativistic energy region.

As mentioned before, only relativistic particles are suited for a fixed rf frequency acceleration scheme in both types of FFAG accelerators. However, if a serpentine acceleration scheme is applied to scaling FFAG [34], high-power beam with c.w. mode and rapid-acceleration can be achieved even in the non-relativistic energy region as well. The purpose of this study is to examine a serpentine acceleration scheme in scaling FFAG both theoretically and practically, allowing fixed rf frequency acceleration in non-relativistic energy region.

1.6   Organization of the study

Basic rf acceleration schemes are discussed in Chapter 2. The Chapter 3 is dedicated to the study of the serpentine acceleration scheme in scaling FFAG. First, longitudinal hamiltonian with fixed rf frequency is derived analytically to analyze longitudinal dynamics in scaling FFAG. The features of serpentine acceleration are studied with longitudinal hamiltonian. Furthermore, in order to suppress the beam energy spread at extraction energy, serpentine acceleration with square wave rf voltage is studied analytically. To demonstrate serpentine acceleration in scaling FFAG, experiments are conducted in electron scaling FFAG ring. Experimental setups are presented and measurement results are discussed with theoretical predictions in Chapter 4. These studies are summarized theoretically and experimentally in Chapter 5. Finally, an example of longitudinal design for ADS proton driver is presented with serpentine acceleration in scaling FFAG in Chapter 6.

Radio frequency acceleration

Charged particles in the accelerators gain energy by the electric field in the longitudinal direction. Since the electric field strength of an electrostatic accelerator is limited by field breakdown and by the length of the acceleration sections, electrostatic accelerators, such as Cockcroft-Walton and Van de Graaff accelerators, have been mainly for low energy acceleration. Alternatively, a radio-frequency (rf) cavity operating in a resonance condition has been developed to provide accelerating voltage with $V \sin(\phi_s + \omega_{rf} t)$, where V is the amplitude of the rf voltage, ϕ_s is a phase factor and ω_{rf} is the angular frequency synchronized with the arrival time of beam particles.

Various methods of beam acceleration with rf frequency have been proposed in circular accelerators. For synchrotron case, a beam acceleration is usually realized with the frequency modulation of the rf system. With this acceleration scheme, energy gain from injection to extraction is not limited by the longitudinal parameters. However the acceleration repetition rate is limited by the capabilities of the rf system, such as rf voltage. Therefore beam intensity is limited by the rf cavity faculties. Another scheme is a beam acceleration with fixed rf frequency. Since continuous wave (c.w.) operation is possible, high-intensity beams can be obtained.

In this chapter, we discuss first the classical approach of synchrotron motion with rf acceleration. Then fundamental principles of phase oscillation and phase stability are discussed. The beam acceleration with modulated rf frequency and fixed rf frequency, i.e. stationary bucket acceleration, are finally described.

2.1   Resonant acceleration

The acceleration process may be studied by considering the standing wave set up in the rf cavity as a series of waves traveling in both directions around the ring. Only the wave which moves synchronously with the beam will produce any net acceleration in the long term. The other waves will sometimes accelerate and sometimes decelerate the beam, but the average effect will produce no net acceleration. To quantify this, we will make a few simplifying assumptions as follows. The acceleration gap of length g is only one in a ring, located at $s = 0$, and the length is much shorter than the distance traveled by the beam during one rf period, $g \ll \beta \lambda_{rf}$ where β is the Lorentz factor and λ_{rf} is the wavelength of the rf field. The rf angular frequency ω_{rf} is assumed to be an integer multiple of the angular revolution frequency ω_s, i.e. $\omega_{rf} = h\omega_s$ with an integer h. Furthermore, when the synchronous particle crossed the rf gap at time $t = 0$, the rf phase is assumed ϕ_s, and the rf voltage at the gap is assumed $V \sin \phi_s$. Thus, the energy gain of synchronous particle per revolution is

$$\Delta U_s = eV_0 \sin \phi_s, \tag{2.1}$$

with the rf peak voltage V_0 and particle charge e. The effective electric field is written as

$$\vec{E}(s,t) = \hat{s}E(s,t) = \hat{s}V_0 \sin(\omega_{rf}t + \phi_s) \sum_{n=-\infty}^{\infty} \delta(s - nL), \tag{2.2}$$

where $\hat{s}$ is the unit vector of s direction, n is an integer and L is the circumference of the synchronous particle's orbit. The delta function may be expanded in a Fourier series, so that

$$
\begin{aligned}
E(s,t) &= \frac{V_0}{L} \sin(\omega_{rf}t + \phi_s) \sum_{n=-\infty}^{\infty} \cos(\frac{2\pi n s}{L}) \\
&= \frac{V_0}{L} \sum_{n=-\infty}^{\infty} \sin\left[\omega_s(ht - \frac{n}{v}s) + \phi_s \right],
\end{aligned}
\tag{2.3}
$$

with the synchronous particle's velocity being $v = L\omega_s/2\pi$. Each term in the last equation 2.3 shows a traveling wave with a different velocity. The same velocity of the synchronous particle is the only wave with $n = h$. This is the

only wave which gives a net acceleration. The period t_s of the synchronous particle with length s is written as

$$t_s = \frac{s}{v},\tag{2.4}$$

and the time t for a non-synchronous particle is

$$t = t_s + \delta t,\tag{2.5}$$

where δt is the amount of time lag from the synchronous particle. If we assume that the longitudinal oscillation have a much lower frequency than the angular revolution frequency ω_s of synchronous particle, the electric field may be averaged over one revolution, giving

$$< E(\delta t) > = \frac{V_0}{L} \sin(\omega_{rf}\delta t + \phi_s),\tag{2.6}$$

for the effective field seen by a non-synchronous particle whose time lag is δt. A non-synchronous particle then gains the energy

$$\Delta U = eV_0 \sin(\omega_{rf}\delta t + \phi_s)\tag{2.7}$$

per turn.

2.2 The phase oscillation equation

The physical quantities related to a non-synchronous particle and to the synchronous one are linked by the following relations:

$$
\begin{aligned}
\text{total energy} U &= U_s + \delta U \\
\text{momentum} p &= p_s + \delta p \\
\text{angular frequency} \omega &= \omega_s + \delta \omega \\
\text{revolution period} t &= t_s + \delta t
\end{aligned}
\tag{2.8}
$$

with $\text{sign}(\delta\omega) = \text{sign}(-\delta t)$. Since the synchronous particle must arrive at the rf cavity gap with the same phase, we may write

$$\omega_{rf} = h\omega_s,\tag{2.9}$$

11

with some integer h called the harmonic number. The phase of the rf voltage when the synchronous particle arrives at the cavity gap is ϕ_s. For the non-synchronous particle, the phase at the cavity gap is ϕ. The relative phase difference between the non-synchronous and synchronous particles is then

$$\psi = \delta\phi = \phi - \phi_s. \tag{2.10}$$

Assuming that the particles pass through the accelerating gap much faster than the rf period, we may define the energy gain of the synchronous and the non-synchronous particle per turn

$$\begin{aligned} \Delta U &= eV_0 \sin\phi, \\ \Delta U_s &= eV_0 \sin\phi_s, \end{aligned} \tag{2.11}$$

respectively. The energy deviation of the non-synchronous particle from that of the synchronous particle at the beginning of the n-th turn is written as

$$(\delta U)_n = U - U_s. \tag{2.12}$$

After the n-th turn the deviation is

$$(\delta U)_{n+1} = (U + \Delta U) - (U_s + \Delta U_s). \tag{2.13}$$

The difference of δU after one turn is then

$$\begin{aligned} \Delta(\delta U) &= (\delta U)_{n+1} - (\delta U)_n \\ &= \Delta U - \Delta U_s = eV_0(\sin\phi - \sin\phi_s). \end{aligned} \tag{2.14}$$

For a slowly varying oscillation about the synchronous energy, we may write

$$\frac{d(\delta U)}{dt} \sim \frac{\Delta(\delta U)}{t_s} = \frac{eV_0}{2\pi}\omega_s(\sin\phi - \sin\phi_s). \tag{2.15}$$

Defining the variable

$$W = \frac{\delta U}{\omega_{rf}}, \tag{2.16}$$

Equation 2.15 becomes

$$\frac{dW}{dt} = \frac{eV_0}{2\pi h}(\sin\phi - \sin\phi_s) \tag{2.17}$$

with Eq. 2.9. Again when the oscillations are slow, after one turn phase difference $\Delta\psi$ is

$$\Delta\psi \sim \frac{d\psi}{dt}t_s = \omega_{rf}\delta t, \tag{2.18}$$

where δt is the difference in the arrival times at the cavity gap of the non-synchronous and synchronous particles. After one turn, the change in δt is

$$\Delta(\delta t) = t - t_s = \delta t. \tag{2.19}$$

Since the revolution period t is expressed by the circumference L and the velocity v, after one revolution the difference in the revolution period δt of the non-synchronous and synchronous particles is written by

$$\frac{\delta t}{t} = \frac{\delta L}{L} - \frac{\delta v}{v} = \left(\alpha - \frac{1}{\gamma^2}\right)\frac{\delta p}{p} = \eta\frac{\delta p}{p}, \tag{2.20}$$

where α is the momentum compaction factor defined by

$$\alpha = \frac{\delta L}{L}\bigg/\frac{\delta p}{p}, \tag{2.21}$$

and η is called the slippage factor defined by

$$\eta = \alpha - \frac{1}{\gamma^2}, \tag{2.22}$$

with the Lorentz factor γ. When $\eta = 0$, the Lorentz factor γ is called the transition gamma γ_t;

$$\gamma_t = \sqrt{1/\alpha}. \tag{2.23}$$

Substituting Eqs. 2.19 and 2.20 into Eq. 2.18 and assuming that the change in δt is small, we have

$$\frac{d\psi}{dt} \sim \frac{\omega_{rf}^2\eta}{\beta^2 U_s}W, \tag{2.24}$$

where the momentum deviation is related to the energy deviation as

$$\frac{dp}{p} = \frac{\delta U}{\beta^2 U}. \tag{2.25}$$

The two first-order differential equations 2.17 and 2.24 can be combined into one second-order equation

$$\frac{d^2\psi}{dt^2} - \frac{h\omega_s^2\eta eV_0}{2\pi\beta^2 U_s}(\sin\phi - \sin\phi_s) = 0. \tag{2.26}$$

2.2.1 Synchrotron tune

For small oscillations of the phase, $\sin \phi = \sin(\phi_s + \psi) \sim \sin \phi_s + \psi \cos \phi_s$, and Eq. 2.26 becomes the equation for a linear harmonic oscillator;

$$\frac{d^2\psi}{dt^2} + \Omega_s^2 \psi = 0, \tag{2.27}$$

with synchrotron oscillation frequency expressed by

$$\Omega_s = \omega_s \sqrt{-\frac{h\eta \cos \phi_s}{2\pi\beta^2} \frac{eV_0}{U_s}}. \tag{2.28}$$

Then synchrotron tune is given by $Q_s = \Omega_s/\omega_s$.

2.3 The phase stability principle

Below the transition energy, i.e. $\gamma < \gamma_t$ and $\eta < 0$, the stability condition is $0 < \phi_s < \pi/2$. In this case the speed of a higher energy particle compensates more than the difference in path length, and particle revolution frequency is higher than synchronous revolution frequency. Thus a particle with higher energy reaches the rf gap earlier than a synchronous particle as shown in Fig. 2.1. On the other hand, above the transition energy, i.e. $\gamma > \gamma_t$ and $\eta > 0$, the phase stability condition is $\pi/2 < \phi_s < \pi$. In this case, particle velocity variation do not compensate trajectory variation, and particle revolution frequency is lower than synchronous revolution frequency. Thus higher particle energy reaches the rf gap later than a synchronous particles as shown in Fig. 2.2. When the particle energy is the transition energy, $\gamma = \gamma_t$, the revolution period is independent on the particle energy. With this condition, all particles at different momenta round a ring at the same period. This is called isochronous condition.
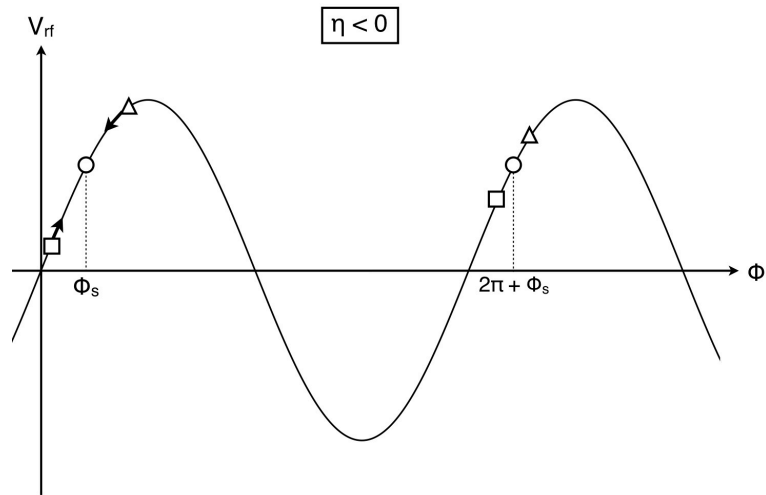
Figure 2.1: The schematic drawing of an rf wave when η is negative. The revolution period of the particle which has higher energy (triangle-shaped figure) than the synchronous particle (round-shape figure) is shorter than that of the synchronous particle. On the other hand, the revolution period of the particle which has lower energy than the synchronous particle (quadrilateral figure) is longer than that of the synchronous particle. This motion is continued until that the non-synchronous particle reaches the synchronous energy.

Figure 2.2: The schematic drawing of an rf wave when η is positive. The revolution period of the particle which has higher energy than the synchronous particle (triangle-shaped figure) is longer than that of the synchronous (round-shape figure). On the other hand, the revolution period of the particle which has a lower energy than the synchronous particle (quadrilateral figure) is shorter than that of the synchronous particle. This motion is continued until that the non-synchronous particle reaches the synchronous energy.
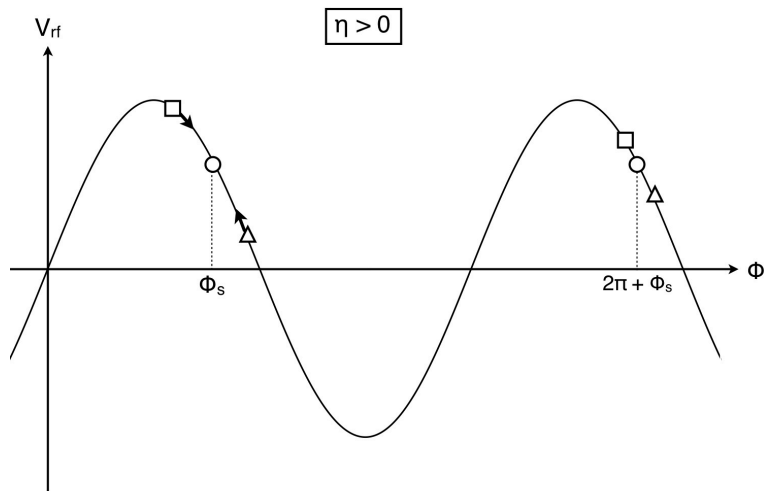
2.4 Hamiltonian formalism

The longitudinal hamiltonian can be derived from the energy and phase equations of motion, i.e. Eqs. 2.17 and 2.24. We choose the energy variable W canonically conjugate to the coordinate variable ϕ. Then hamiltonian satisfies Hamilton's equations with

$$\frac{dW}{dt} = -\frac{\partial H}{\partial \phi} = \frac{eV_0}{2\pi h}[\sin\phi - \sin\phi_s], \text{ and}$$

$$\frac{d\phi}{dt} = \frac{\partial H}{\partial W} = \frac{\omega_{rf}^2 \eta}{2\beta^2 U_s} W. \tag{2.29}$$

An obvious solution to this pair of equations is

$$H(W,\phi) = \frac{\omega_{rf}^2 \eta}{2\beta^2 U_s} W^2 + \frac{eV_0}{2\pi h}[\cos\phi - \cos\phi_s + (\phi - \phi_s)\sin\phi_s]. \tag{2.30}$$

For a small amplitudes Eq 2.30 becomes

$$H \sim \frac{\omega_{rf}^2 \eta}{2\beta^2 U_s} W^2 - \frac{eV_0 \cos\phi_s}{4\pi h}(\phi - \phi_s)^2, \tag{2.31}$$

which is just the Hamiltonian for a harmonic oscillator.

2.5 Beam acceleration

As we mentioned before, two types of beam acceleration using an rf cavity have been proposed in scaling FFAG so far. One is an ordinary method where beam acceleration is realized with frequency modulation of the rf system. Another scheme is stationary bucket acceleration where rf frequency is fixed.

In this section, before the details of two types of rf acceleration schemes are discussed, bucket height is derived analytically.

2.5.1 Bucket height

The point where $H(W,\phi) = H(0,\phi_s)$ is called the stable fixed point. The other points where $H(W,\phi) = H(0,\pi - \phi_s) = H(0,\phi_2)$ are unstable fixed points. The point where $H(0,\phi_2)$ is a solution to the transcendental equation

$$\cos\phi_2 + \cos\phi_s + (\phi_2 + \phi_s - \pi)\sin\phi_s = 0, \tag{2.32}$$

which is easily obtainable from Eq. 2.30. The torus that passes through the unstable fixed point is called separatrix; it separates phase space in to regions of bound and unbound oscillations. Figure 2.3 and 2.4 show the separatrix orbits below and above transition with different synchronous phases. The synchronous phase space is divided into stable and unstable regions. Particles outside the rf bucket drift along the longitudinal direction. Only particles in the stable region can be accelerated to high energy.

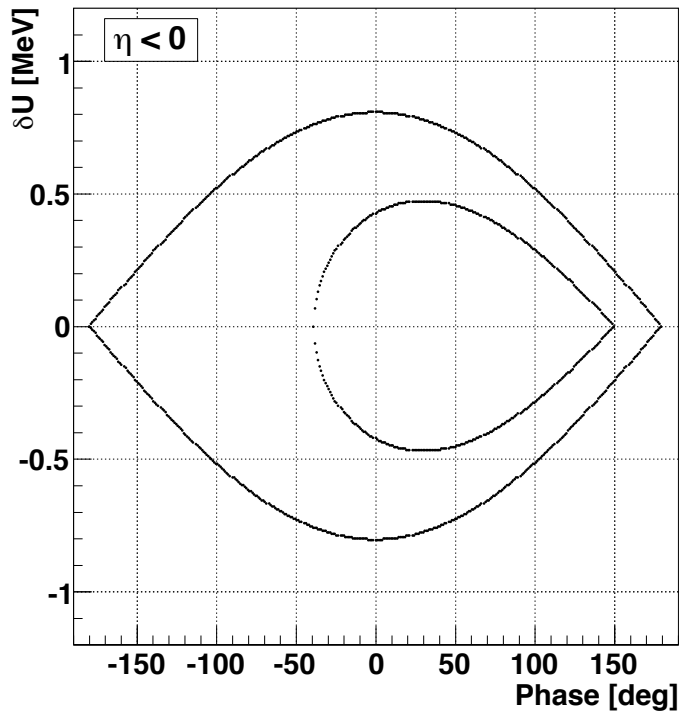Figure 2.3: Separatrix orbits for the stationary bucket ($\phi_s = 0°$) and an accelerating bucket ($\phi_s = 30°$) for below transition, $\eta < 0$. Horizontal axis indicates non-synchronous particle phase ϕ, and vertical axis indicates energy differences from the synchronous energy. For the stationary bucket, when the rf phase is $2\pi n$ (n is an integer), the rf bucket height is maximum.

Figure 2.4: Separatrix orbits for the stationary bucket ($\phi_s = 180°$) and an accelerating bucket ($\phi_s = 150°$) for above transition ($\eta > 0$). Horizontal axis indicates non-synchronous particle phase ϕ, and vertical axis indicates energy differences from the synchronous energy. For the stationary bucket, when the rf phase is $n\pi$ (n is an integer), the rf bucket height is maximum.
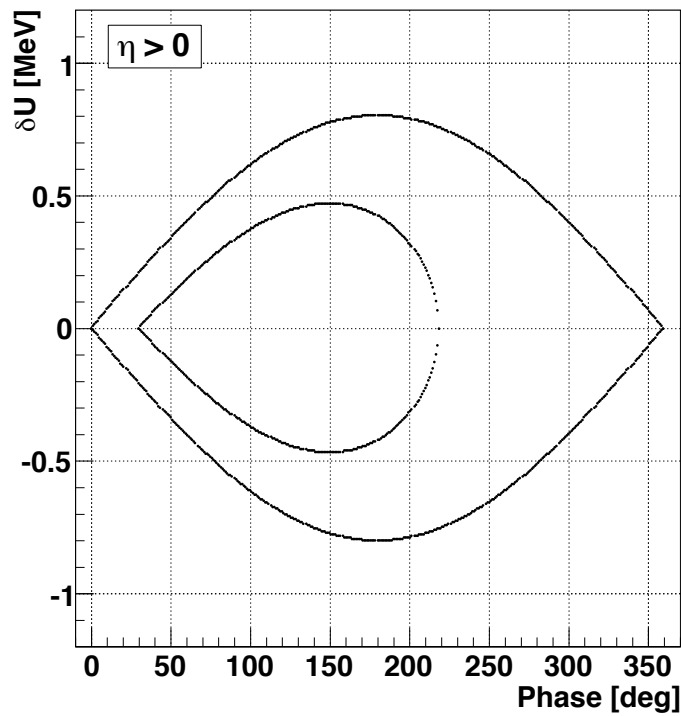
Energy deviation of separatrix is derived from Eq. 2.24 and 2.26 as:

$$\delta U_{sep} = \sqrt{-\frac{\beta^2 E_s}{\pi h \eta} e V_0 [\cos(\phi_s + \psi) + \phi \sin \phi_s]_{\psi=\psi_m}^{\psi}}, \qquad (2.33)$$

and the phase-space area enclosed by the separatrix is called an rf bucket in longitudinal phase space.

There are two kinds of rf buckets. One is called a stationary bucket where the synchronous phase is zero or π. The other are called a moving bucket where the synchronous phase is finite value different from zero or π. Since non-synchronous particles oscillate around the synchronous particle in the rf bucket, bunched beam is formed around the synchronous particle. A beam in which particles are grouped together forming bunches is called a bunched beam. The phase-space area enclosed by the separatrix orbit is called the bucket area.

2.5.2   Frequency-modulated acceleration

The beam acceleration using modulated rf frequency scheme is the ordinary method for beam acceleration in synchrotron. Since synchronous phase is not zero in this scheme, not only non-synchronous but synchronous particle gains energy at the rf cavity. Thus the revolution frequency of the synchronous particle is changing during beam acceleration. For this reason, the rf frequency is modulated in order to provide an appropriate acceleration scheme as shown in Fig. 2.5 and 2.6.

With this scheme, beam can be ideally accelerated up to any energy. However the successive beam cannot be injected until the former beam is extracted from the ring. Thus the acceleration repetition rate is limited by the capabilities of the rf system such as obtaining a high enough rf voltage.

This modulated rf frequency acceleration scheme is not suitable in the case of rapid acceleration of short-lived particles like muons. Furthermore, since c.w. operation cannot be achieved, beam intensity is limited by the capability of a rf cavity.
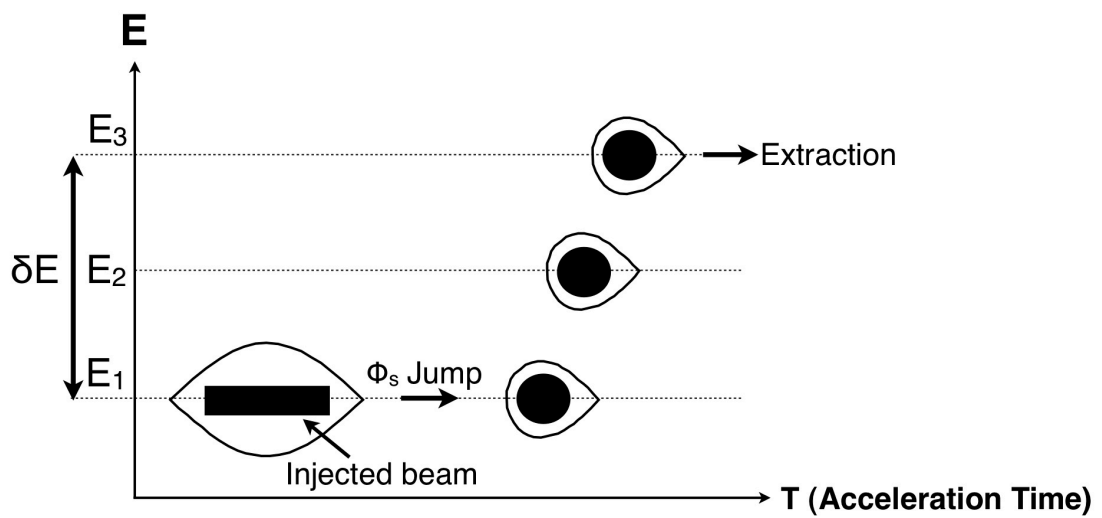
Figure 2.5: The schematic view of a modulated rf acceleration scheme. Injected beam is captured by the stationary bucket. After synchronous phase ϕ_s jump, the bunched beam can be accelerated with modulated rf frequency. All synchronous energies E_1, E_2 and E_3 correspond to each rf frequency. The total energy gain from injection to extraction is presented by δE.
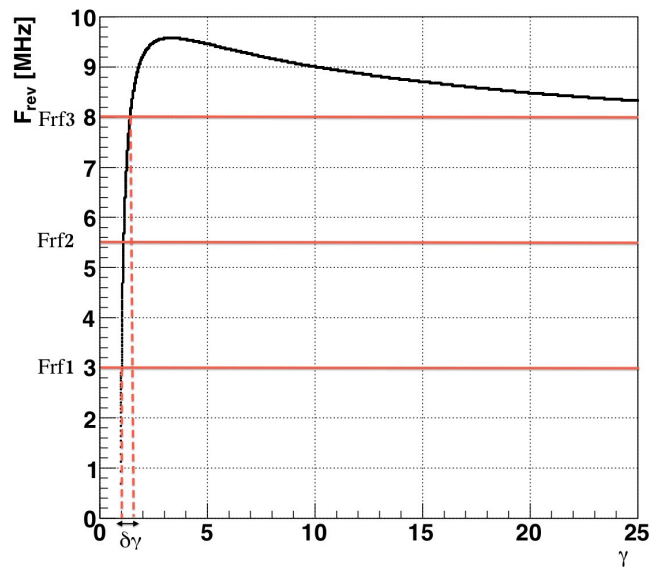
Figure 2.6: An example of the relation between particle energy and revolution frequency of non-synchronous particle. Horizontal axis indicates beam energy. Rf frequency at the injection is presented by F_{rf1}. Rf frequencies F_{rf2} and F_{rf3} correspond to the E_2 and E_3 in Fig. 2.5. The total energy gain from injection to extraction is indicated by $\delta\gamma$.

2.5.3 Fixed rf acceleration

Fixed rf acceleration scheme is mainly used for linear accelerators and cyclotrons so far. However in scaling FFAG, the fixed rf acceleration scheme called stationary bucket acceleration has been proposed for a muon accelerator [28, 36].

The advantage of a stationary bucket acceleration scheme is high intensity beams can be obtained because beams can be injected and accelerated with c.w. operation as shown in Fig. 2.7. Furthermore, since we fixed a rf frequency during beam acceleration as shown in Fig. 2.8, fast acceleration with high repetition rate can be also achieved. Thus a stationary bucket acceleration scheme is suitable for a short-lived particle acceleration, such as muons. However, since beams can be accelerated only in a stationary bucket, the total energy gain from injection to extraction is limited by a bucket height. In order to increase a energy gain between injection to extraction, it is necessary to obtain big enough rf bucket.

From Eq. 2.33, the maximum energy differences δU_{max} of the separatrix orbit is called the bucket height;

$$\delta U_{max} = \sqrt{-\frac{2\beta_s^2 E_s}{\pi h \eta} eV_0 [\cos\phi_s - (\frac{\pi}{2} - \phi_s)\sin\phi_s]}. \qquad (2.34)$$

Referring to Eq. 2.34, big rf peak voltage V_0 per harmonic number h, high stationary energy E_s and small slippage factor η are desired to make a large bucket height. Since a high stationary energy is preferable, the beam acceleration in relativistic energy region is required.

Since a bucket height is large in a stationary bucket acceleration scheme, energy deviation and phase deviation between non-synchronous particle and synchronous particle per turn is not small. Thus the classical approach of synchrotron motion is not accurate. For this reason, it is necessary to develop the synchrotron motion without approximation on the energy and phase variation.
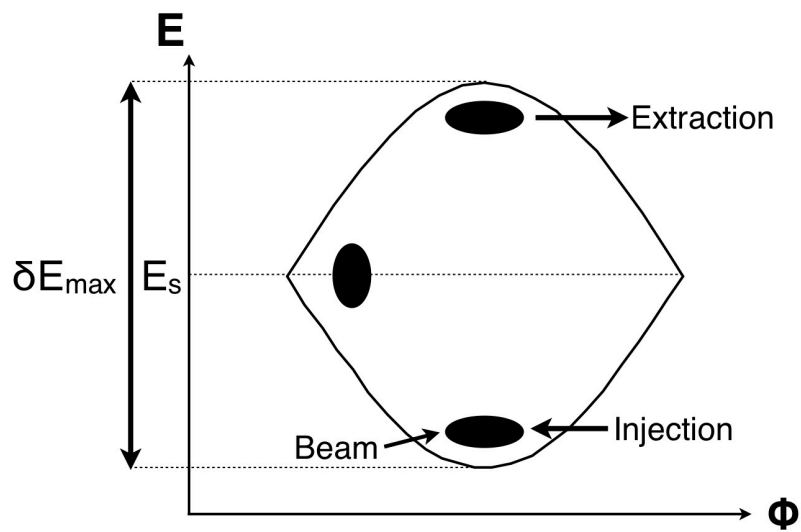
Figure 2.7: Schematic view of a fixed rf acceleration scheme. A beam is injected at the bottom of a stationary bucket. Then the injected beam is accelerated in the stationary bucket. When the beam reaches the top of its energy, it is extracted from the stationary bucket. The synchronous energy is E_s, and maximum energy gain is presented by δE_{max} from injection to extraction.
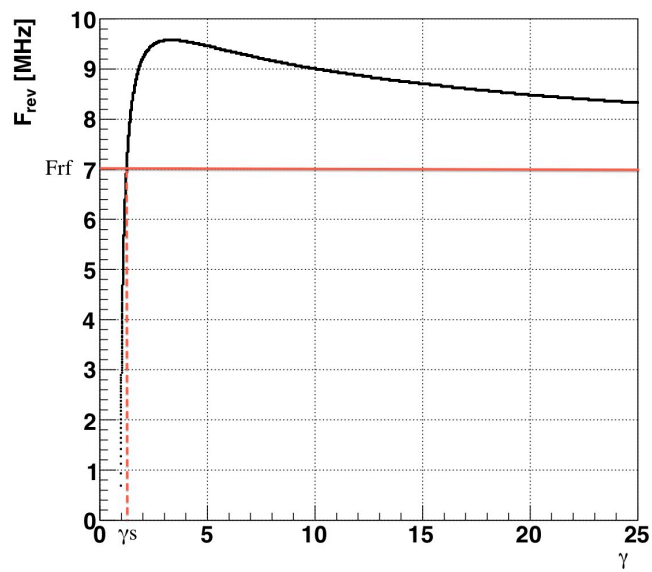
Figure 2.8: An example of the relation between particle energy and revolution frequency of non-synchronous particle. Horizontal axis is beam energy. The rf frequency is presented as F_{rf}. Lorentz factor γ_s is corresponding to the synchronous energy. Since the synchronous energy is fixed, a beam is only accelerated in a stationary bucket.

Serpentine acceleration in scaling FFAG accelerator

In scaling FFAG, the fixed rf acceleration scheme called stationary bucket acceleration has been proposed [28, 35, 36]. However, with this scheme, total energy gain from injection to extraction is limited by a bucket height. Thus a bucket height must be high enough to cover the required energy range. To satisfy this requirement, the beam acceleration with stationary bucket acceleration is useful in relativistic energy region. In order to accelerate beam with fixed rf acceleration not only in relativistic but non-relativistic energy region, we propose a new type of beam acceleration, so-called serpentine acceleration, in scaling FFAG.

Serpentine acceleration has been proposed in non-scaling FFAG so far. However only relativistic particles are suited in this type of accelerator. On the other hand in scaling FFAG, with the appropriate selection of momentum compaction factor α, not only relativistic but non-relativistic particles can be accelerated with a serpentine acceleration scheme [34, 37, 38, 39, 40, 41].

Classically we consider that the energy and phase deviations between synchronous and non-synchronous particles are small, presented in Chapter. 2. In this case, linearized synchrotron motion can be obtained analytically. However, in a serpentine acceleration scheme, energy range between injection to extraction becomes large. Thus energy and phase deviation of non-synchronous particles from synchronous particles are not small. Since the classical approach of the linearized synchrotron motion is not accurate anymore, we need to develop the synchrotron motion without linear approximation.

In this chapter, first the longitudinal hamiltonian with fixed rf frequency is derived analytically without linear approximation on the phase and energy deviations. Lowest limit of rf voltage, called minimum rf voltage, to make a serpentine channel is also derived with longitudinal hamiltonian. Further-

more, the total energy gain from injection to extraction and the longitudinal phase acceptance are studied. The idea of applying a square rf voltage wave form is considered in beam acceleration finally. We use the convention of the light velocity $c = 1$ in this chapter.

3.1 Longitudinal beam dynamics in scaling FFAG with fixed rf acceleration

In Chapter 2, we have already discussed the particle motions in the linear approximation and derive the longitudinal hamiltonian to the first order in momentum deviation from the synchronous particle. However the aim of this section is to study the exact particle motions in scaling FFAG, using rigid conditions between particle momentum and revolution period.

In scaling FFAG, the relation between the equivalent mean radius R and the momentum P is exactly given by

$$R = R_0 \left(\frac{P}{P_0} \right)^{\frac{1}{k+1}},\tag{3.1}$$

where R_0 is the equivalent mean radius at the momentum P_0, and k is the geometrical field index. Details are discussed in App. A.

In longitudinal particle dynamics with constant rf frequency, the phase differences per revolution $\Delta\phi$ of a non-synchronous particle is written as

$$\Delta\phi = 2\pi(f_{rf} \cdot T - h),\tag{3.2}$$

where h is the integer called harmonic number, f_{rf} is the rf frequency and T is the revolution period of the non-synchronous particle. The revolution frequency f_s of synchronous particle is expressed with the rf frequency f_{rf} as follows

$$f_{rf} = h \cdot f_s.\tag{3.3}$$

Using Eq. 3.3, Eq. 3.2 becomes

$$\frac{\Delta\phi}{2\pi} = \frac{hT}{T_s} - h.\tag{3.4}$$

Equation 3.4 can be also expressed with another description based on Eq. 3.2 as follows

$$
\begin{aligned}
\frac{T}{T_s} = 1 + \frac{\Delta\phi}{2\pi h} &= \left(\frac{R}{R_s}\right) \bigg/ \frac{P/E}{P_s/E_s} \\
&= \left(\frac{P}{P_s}\right)^\alpha \frac{P_s}{E_s} \left(\frac{E^2}{E^2 - m^2}\right)^{\frac{1}{2}} \\
&= \left(\frac{E^2 - m^2}{P_s^2}\right)^{\frac{\alpha}{2}} \frac{P_s}{E_s} \left(\frac{E^2}{E^2 - m^2}\right)^{\frac{1}{2}} \\
&= (E_s^2 - m^2)^{\frac{1-\alpha}{2}} \frac{E}{E_s} (E^2 - m^2)^{\frac{\alpha-1}{2}},
\end{aligned}
\tag{3.5}
$$

where $\alpha = 1/(k+1)$ is the momentum compaction factor, E_s is the stationary energy, R_s is the equivalent mean radius of the synchronous particle, and m is the rest mass.

To describe the momentum compaction factor in scaling FFAG, we first introduce a transverse motion in scaling FFAG. The equivalent mean radius R of the closed orbit for the momentum P is defined by

$$
R = \frac{L}{2\pi},
\tag{3.6}
$$

with the circumference L. From Eq. 3.6, we have

$$
\frac{\Delta L}{L} = \frac{\Delta R}{R}.
\tag{3.7}
$$

The vertical magnetic field B_z in the mid-plane in scaling FFAG is

$$
B_z = B_{z,0} \left(\frac{R}{R_0}\right)^k \mathcal{F},
\tag{3.8}
$$

where $B_{z,0}$ is the vertical magnetic field at the radius of R_0, k is the constant geometrical field index and $\mathcal{F}$ is the arbitrary function describing the dependence on the azimuthal coordinate.

The particle momentum P on the closed orbit of the equivalent mean radius R can be expressed from Eq. 3.8 as

$$
P = P_0 \left(\frac{R}{R_0}\right)^{k+1},
\tag{3.9}
$$

where P_0 is the momentum for the closed orbit of the equivalent mean radius R_0. Then, the relation between momentum deviation ΔP and deviation of equivalent mean radius ΔR can be expressed as

$$\frac{\Delta P}{P} = (k+1)\frac{\Delta R}{R}, \tag{3.10}$$

and we can get

$$\frac{\Delta R/R}{\Delta P/P} = \frac{1}{k+1}. \tag{3.11}$$

From Eq. 2.21 with Eqs. 3.7 and 3.11, the momentum compaction factor α in scaling FFAG is thus

$$\alpha = \frac{1}{k+1}. \tag{3.12}$$

From Eq. 3.12, the momentum compaction factor α in scaling FFAG is determined only by the k-value and independent of particle momentum. Then the transition energy γ_t in scaling FFAG is defined as

$$\gamma_t = \sqrt{(k+1)}. \tag{3.13}$$

Combining Eqs. 3.4 and 3.5, the phase difference $\Delta\phi$ per turn is

$$\Delta\phi = 2\pi h \left[\frac{(E_s^2 - m^2)^{\frac{1-\alpha}{2}}}{E_s} E(E^2 - m^2)^{\frac{\alpha-1}{2}} - 1 \right]. \tag{3.14}$$

Now we assume that many rf cavities are considered to be uniformly distributed in the ring. It means that the energy gain and phase deviation are small for each passage in a rf cavity. From this assumption, $\Delta\phi/2\pi$ can be approximated by $d\phi/d\Theta$ to derive the phase equation of motion;

$$\frac{d\phi}{d\Theta} = h \left[\frac{(E_s^2 - m^2)^{\frac{1-\alpha}{2}}}{E_s} E(E^2 - m^2)^{\frac{\alpha-1}{2}} - 1 \right], \tag{3.15}$$

where Θ is the equivalent azimuthal angle associated to the equivalent mean radius R in the machine.

The energy gain ΔE per turn of a non-synchronous particle can be expressed as

$$\Delta E = eV_0 \sin\phi, \tag{3.16}$$

where V_0 is the rf gap peak voltage. Here also $\Delta E/2\pi$ is exchanged by $dE/d\Theta$ to derive the energy equation of motion:

$$\frac{dE}{d\Theta} = \frac{eV_0}{2\pi}\sin\phi. \tag{3.17}$$

We choose the energy variable E canonically conjugate to the coordinate variable ϕ. Then the longitudinal hamiltonian with constant rf frequency is derived with Eqs. 3.15 and 3.17 as:

$$H(E, \phi; \Theta) = h \left[\frac{1}{\alpha + 1} \frac{(E^2 - m^2)^{\frac{\alpha+1}{2}}}{E_s(E_s^2 - m^2)^{\frac{\alpha-1}{2}}} - E \right] + \frac{eV_0}{2\pi} \cos \phi. \qquad (3.18)$$

3.2 Serpentine acceleration

Below the transition energy, the velocity variation over compensates the circumference variation. In this case the revolution frequency of non-synchronous particle increases with energy. On the other hand, above the transition energy, the velocity variation does not compensate the circumference variation. Then the revolution frequency of non-synchronous particle decreases with energy. Thus when the rf frequency is fixed, two stationary energies are determined as presented in Fig. 3.1; one is below the transition energy and the other one is above the transition energy. If both stationary energies, i.e. stationary buckets, are close to each other, the channel called serpentine channel appears between both stationary buckets. Injected beam in the serpentine channel can be accelerated around both stationary buckets. Therefore, total energy gain with serpentine acceleration is bigger than the stationary bucket acceleration. Longitudinal phase space in serpentine acceleration is shown later.

3.3 Longitudinal phase space

With the longitudinal hamiltonian contours expressed by Eq. 3.18, exact particle motions in longitudinal phase space can be expressed even with large energy deviation per turn. In this section, the serpentine acceleration in the longitudinal phase space are presented with hamiltonian contours. First longitudinal phase space with the rf frequency fixed far away from the transition energy is shown. In this case, two stationary buckets are separated. The longitudinal phase space with the rf frequency fixed near the transition energy is represented later. In this case, two stationary buckets are close to each other. Finally, longitudinal phase space with serpentine channels is presented.
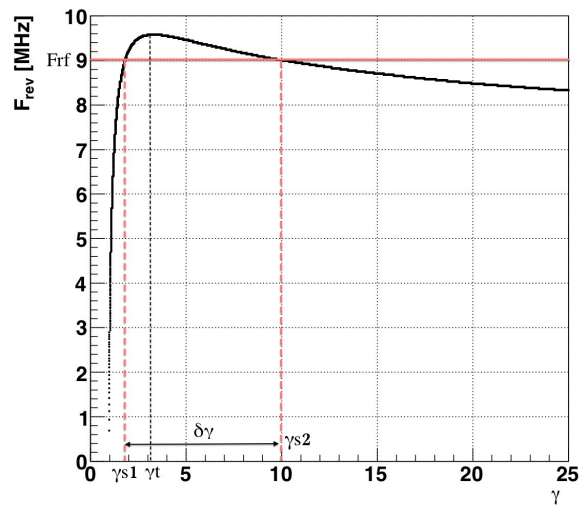
Figure 3.1: Revolution frequency and its energy of a non-synchronous parti-
cle. Lorentz factor γ_t is the transition gamma. Lorentz factor γ_{s1} corresponds
to the stationary energy which is below the transition energy. Lorentz factor
γ_{s2} corresponds to the other stationary energy which is above the transition
energy. Energy deviations between E_{s1} and E_{s2} are indicated by $\delta\gamma$.

3.3.1 Separated stationary buckets

When the rf frequency is fixed far away from the transition energy, two stationary buckets are separated as shown in Fig. 3.2. In this case, serpentine channel does not appear. Then, beam can be accelerated stably only in stationary buckets. Since the stationary energy E_{s2} above the transition energy is bigger than the stationary energy E_{s1} below the transition energy, the bucket height over the transition energy is bigger than the bucket height below the transition energy.
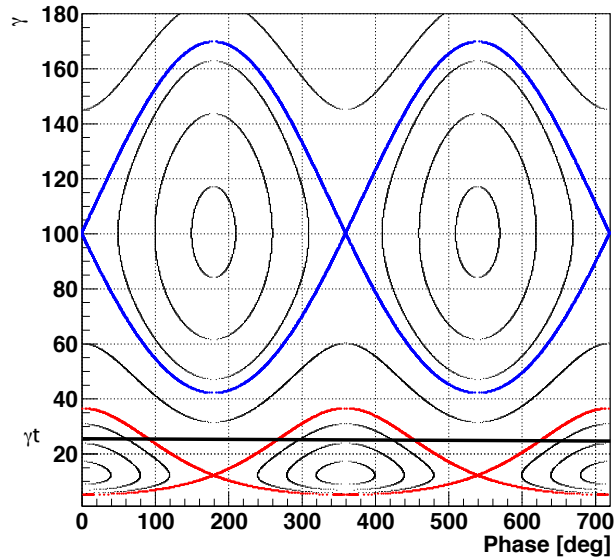

Figure 3.2: Longitudinal phase space with longitudinal hamiltonian contours. Lorentz factor γ_t is the transition gamma. The blue and red contours are the separatrices above and below the transition energy. The synchronous phase below the transition energy is $2n\pi$ (n is an integer) and unstable fixed points are $(2n+1)\pi$ (n is an integer). On the other hand, the synchronous phases above the transition energy are $(2n+1)\pi$ (n is an integer). Unstable fixed points are $2n\pi$ (n is an integer) in this case.

3.3.2   Near the transition energy

When the rf frequency is fixed near the transition energy, two stationary energies, E_{s1} and E_{s2}, are close to each other as shown in Fig. 3.3. When E_{s1} and E_{s2} get closer, the serpentine channel appears between the two stationary buckets as shown in Fig. 3.4. When the rf frequency is fixed much nearer the transition energy, eventually both stationary energies are equal to the transition energy, $E_{s1} = E_{s2} = E_t$. Then, two stationary energies are overlapped to the transition energy as shown in Fig. 3.5.

As presented in Fig. 3.4, since beams can be accelerated with serpentine channel, the total energy gain from injection to extraction is larger than the stationary bucket acceleration. Furthermore, since fixed rf frequency is applied for beam acceleration, we can use a high-quality cavity called high-Q cavity where power loss in the cavity is smaller. Thus, big rf voltage can be obtained compared to the modulated type of rf frequency cavity. Details of a rf cavity is discussed in Appendix B.
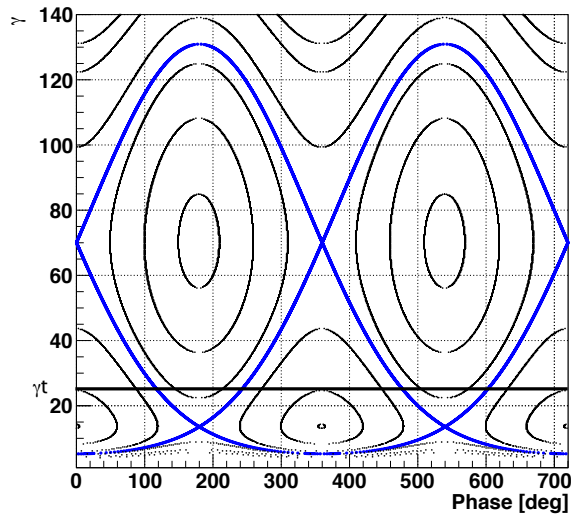

Figure 3.3: Longitudinal phase space. Lorentz factor γ_t is the transition energy. Blue contour indicates separatrix.
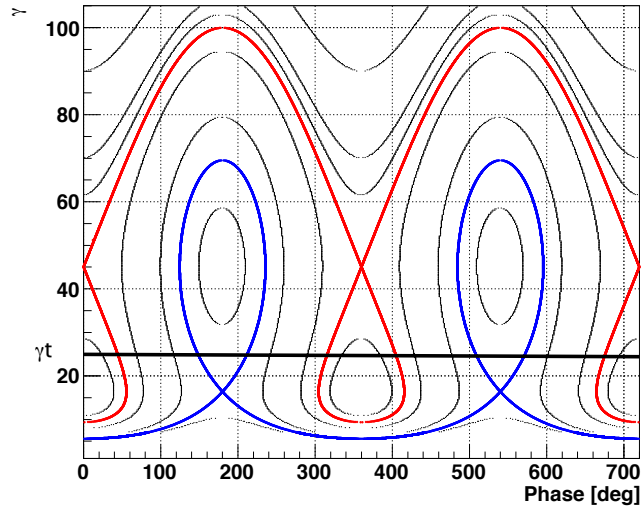
Figure 3.4: Longitudinal phase space near the transition energy. Blue and red lines indicate the separatrices above and below the transition energy.
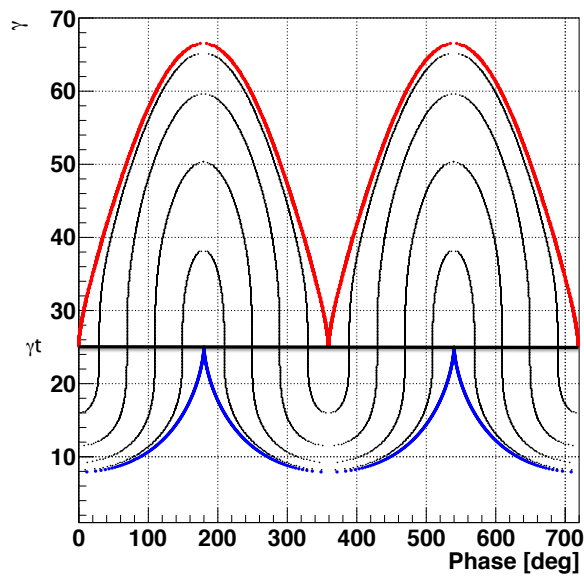

Figure 3.5: Longitudinal phase space near the transition energy. Blue and red lines indicate the separatrices above and below the transition energy.

3.3.3 Serpentine acceleration in non-relativistic energy region

Since injected beam passes through the transition energy with serpentine acceleration, the sign of slippage factor needs to be changed during beam acceleration. As defined in Eq. 2.22, the slippage factor is related to the momentum compaction factor and beam energy. In scaling FFAG, the transition energy, i.e. momentum compaction factor, can be fixed not only in relativistic energy region but also in non-relativistic energy region with the appropriate selection of k-value. Thus the sign of slippage factor for non-relativistic particles can be changed during acceleration. Then non-relativistic particles are accelerated with serpentine acceleration in scaling FFAG. An example of longitudinal design with serpentine acceleration in non-relativistic energy region is shown in Fig. 3.6. Parameters are presented in Tab. 3.1.
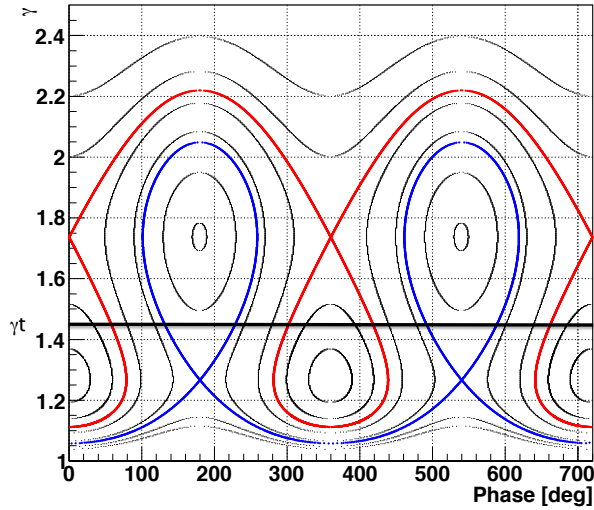

Figure 3.6: Longitudinal phase space in non-relativistic energy region. Blue and red lines indicate separatrices above and below the transition energy respectively. Horizontal axis is the rf phase, and vertical axis indicates beam energy presented by the Lorentz factor γ.

Table 3.1: Longitudinal parameters

k-value	1.1
Transition gamma	1.45
Equivalent mean radius at $\gamma = 1.21$ [m]	10
Stationary gamma below transition	1.27
Rf voltage [MV/turn]	50 ($h=1$)
Rf frequency [MHz]	2.8($h=1$)

3.4 Features of serpentine acceleration

Features of serpentine acceleration are studied in this section. First, the relation between the stationary energy E_{s1} below the transition energy and the other stationary energy E_{s2} above the transition energy are expressed. Then lower limit of the rf voltage to make a serpentine channel is derived from the longitudinal hamiltonian analytically. Total acceleration energy gain and phase acceptance of serpentine acceleration are finally discussed.

3.4.1 Stationary energies and k-value

Let us start from deriving the relation between both stationary energies E_{s1} and E_{s2}. Synchronous particles below and above the transition energy have the same revolution frequency expressed as

$$\frac{\beta_{s1}}{C_{s1}} = \frac{\beta_{s2}}{C_{s2}},\tag{3.19}$$

where β_{s1} and β_{s2} are the Lorentz factor corresponding to the stationary energies E_{s1} and E_{s2} respectively, and C_{s1} and C_{s2} are circumferences of the synchronous particles. Correlation between the stationary energies E_{s1} and E_{s2} are obtained by solving Eq. 3.19 as

$$E_{s1}P_{s1}^{\alpha-1} = E_{s2}P_{s2}^{\alpha-1},\tag{3.20}$$

with the momentum compaction factor α, the rest mass m and the stationary momentum P_{s1} and P_{s2} below and above the transition energy respectively. Once we determine one stationary energy and k-value, the other stationary energy is obtained from Eq. 3.20. The energy difference between the

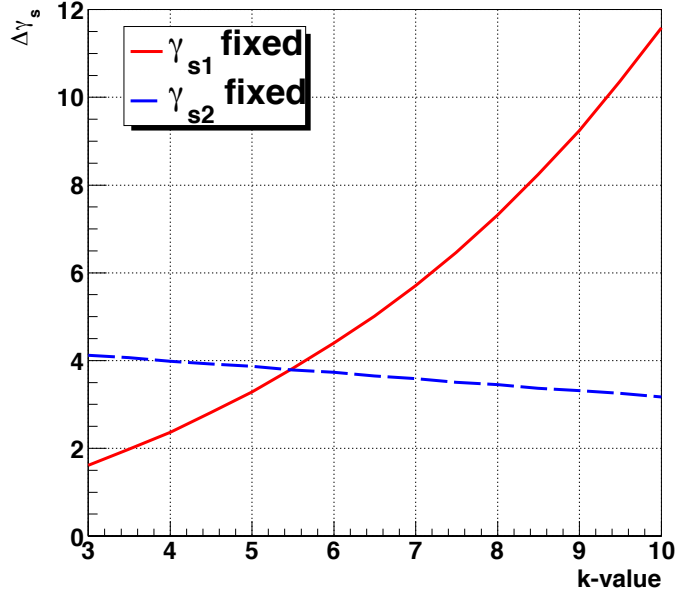stationary energies E_{s1} and E_{s2} with k-value is shown in Fig. 3.7.

Figure 3.7: Correlation between energy deviation $\Delta\gamma_s$ of both stationary energies and k-value. Lorentz factors γ_{s1} and γ_{s2} corresponds to E_{s1} and E_{s2} respectively. Red line indicates the result when γ_{s1} is fixed. Blue dot line indicates the result when γ_{s2} is fixed.

The transition gamma γ_t is increased with k-value. Then, if the stationary energy E_{s1} below the transition energy is kept constant while k-value is increased, the other stationary energy E_{s2} above the transition energy is increased as expressed in Eq. 3.20. Thus, energy difference between the stationary energies E_{s1} and E_{s2} becomes large. On the other hand, when the stationary energy E_{s2} above the transition energy is kept constant while k-value is increased, the other stationary energy E_{s1} below the transition energy is increased. In this case, both stationary energies are close to each other, and energy difference between the stationary energies E_{s1} and E_{s2} becomes small.

3.4.2 Minimum rf voltage to make serpentine channel

Even if rf frequency is fixed near the transition energy and both stationary energies are close to each other, beam cannot be accelerated in serpentine channel without enough rf voltage to make a serpentine channel. It is useful to know the lowest limit of rf voltage to make a serpentine channel when we consider the beam acceleration. In this subsection, the minimum rf voltage to make a serpentine channel is studied.

As shown in Fig. 3.3, the separatrix on the limit condition passes at the two unstable fixed points where $H(E_{s1}, \pi)$ and $H(E_{s2}, 0)$. Then we get the relation written as

$$H(E_{s1}, \pi) = H(E_{s2}, 0), \tag{3.21}$$

where E_{s1} is the stationary energy below the transition energy and E_{s2} is the stationary energy above the transition energy. From Eqs. 3.20 and 3.21, the minimum rf voltage V_{min} to make a serpentine channel can be obtained as

$$V_{min} = \pi h \left[\frac{1}{\alpha + 1} \left(\frac{P_{s1}^2}{E_{s1}} - \frac{P_{s2}^2}{E_{s2}} \right) + (E_{s2} - E_{s1}) \right], \tag{3.22}$$

with the stationary momentum P_{s1} and P_{s2} below and above the transition energy respectively. Equation 3.22 shows that once the k-value, the harmonic number h and the stationary energies E_{s1} and E_{s2} are given, the minimum rf voltage V_{min} can be obtained. Figure 3.8 shows that the correlation between the minimum rf voltage V_{min} and the energy difference between E_{s1} and E_{s2} with fixed harmonic number h and the momentum compaction factor α. From this figure, the larger energy difference between E_{s1} and E_{s2}, the larger minimum rf voltage is required.

3.4.3 Total energy gain of serpentine channel

Total energy gain ΔE_{acc} from injection to extraction in serpentine acceleration is determined by the maximum energy range of the serpentine channel. The maximum energy range of serpentine channel is given by the minimum energy E_{min} and the maximum energy E_{max} of serpentine channel as presented in Fig. 3.9.

From Fig. 3.9, the maximum energy E_{max} passes the unstable fixed point where $H(E_{s2}, 0)$. On the other hand, the minimum energy E_{min} passes the
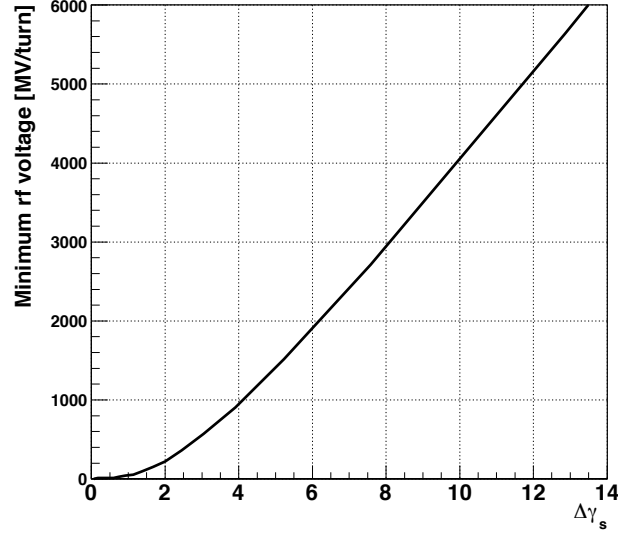
Figure 3.8: Correlation between the minimum rf voltage to make a serpentine channel and energy deviation $\Delta\gamma_s$ between γ_{s1} and γ_{s2}. Lorentz factor γ_{s1} and γ_{s2} correspond to E_{s1} and E_{s2}. In this figure, k-value is 3, and the harmonic number h is 1.

unstable fixed point where $H(E_{s1}, \pi)$. Then we get the relation written as

$$
\begin{aligned}
H(E_{max}, \pi) &= H(E_{s2}, 0), \text{and} \\
H(E_{min}, 0) &= H(E_{s1}, \pi).
\end{aligned}
\tag{3.23}
$$

From Eqs. 3.18, 3.20 and 3.23, the maximum energy E_{max} and the minimum energy E_{min} can be described as

$$
\frac{1}{1+\alpha}\frac{P_{max}^{(\alpha+1)}}{E_{s1}P_{s1}^{(\alpha-1)}} - E_{max} = \left(\frac{1}{1+\alpha}\frac{P_{s2}^2}{E_{s2}} - E_{s2}\right) + \frac{eV_0}{\pi h}, \text{and}
$$

$$
\tag{3.24}
$$

$$
\frac{1}{1+\alpha}\frac{P_{min}^{(\alpha+1)}}{E_{s1}P_{s1}^{(\alpha-1)}} - E_{min} = \left(\frac{1}{1+\alpha}\frac{P_{s1}^2}{E_{s1}} - E_{s1}\right) - \frac{eV_0}{\pi h}.
$$

Then total energy gain ΔE_{acc} can be obtained by solving Eq. 3.24 numerically.
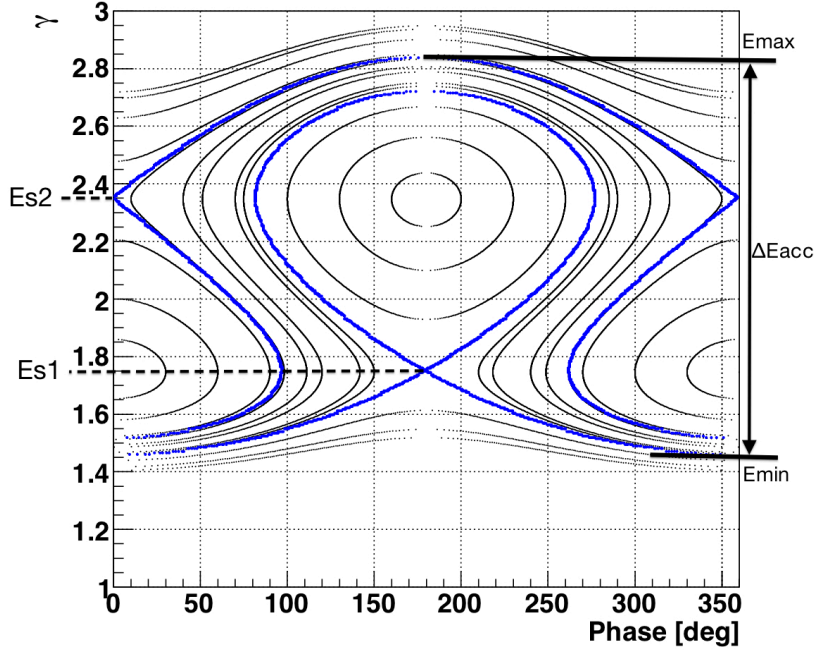
Figure 3.9: Longitudinal phase space with definition of the maximum energy E_{max} and the minimum energy E_{min} of serpentine channel. Blue lines indicate separatrices. The total energy gain ΔE_{acc} is defined by the energy deviation between the energies E_{min} and E_{max}. In this figure, k-value is 3, and the harmonic number h is 1.

For simplicity, let us focus on the relation between the total energy gain ΔE_{acc} and the rf peak voltage V_0 with fixed harmonic number h, k-value and stationary energies E_{s1} and E_{s2} in Eq. 3.24.

Since the bucket height becomes large when the rf voltage is increased, the maximum energy E_{max} of serpentine channel is increased. On the other hand, the minimum energy E_{min} of serpentine channel is decreased. Thus, as shown in Fig. 3.10, the total energy gain E_{acc} becomes large when the rf voltage is increased.

3.4.4 Phase acceptance of serpentine channel

Phase acceptance $\Delta\phi_{acc}$ is also important parameter to determine a pulse length of injected beam in the longitudinal direction. Thus, phase acceptance
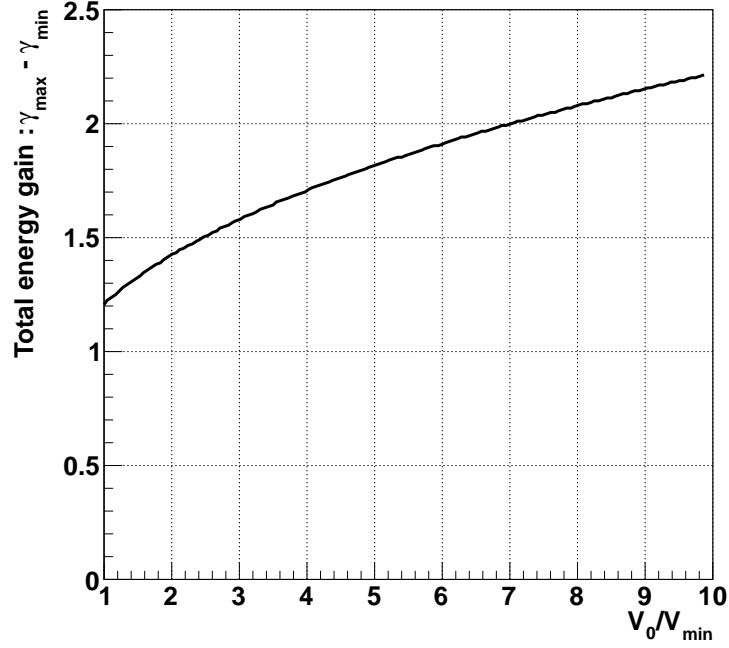
Figure 3.10: Total energy gain ΔE_{acc} and the peak rf voltage V_0 normalized by the fixed minimum rf voltage V_{min}. Total energy gain E_{acc} is expressed by $\gamma_{max} - \gamma_{min}$. Lorentz factors γ_{max} and γ_{min} correspond to the maximum energy E_{max} and the minimum energy E_{min} respectively. In this figure, k-value is 3, and the harmonic number h is 1.

at the stationary energy E_{s1} below the transition energy is examined.

Since the separatrix which has the point where $H(E_{s1}, \phi)$ passes at the unstable fixed point where $H(E_{s2}, 0)$ as shown in Fig. 3.11, $H(E_{s1}, \phi) = H(E_{s2}, 0)$ is obtained. Then the phase ϕ at the stationary energy E_{s1} is written by

$$
\phi = \arccos\left[\frac{2\pi h}{eV_0}\left(\frac{1}{1+\alpha}\left(\frac{P_{s2}^2}{E_{s2}} - \frac{P_{s1}^2}{E_{s1}}\right) + (E_{s1} - E_{s2})\right) + 1\right]
$$
$$
= \arccos\left[\frac{V_0 - 2V_{min}}{V_0}\right],
$$

(3.25)

with the minimum rf voltage V_{min} written in Eq. 3.22. Therefore, the phase acceptance $\Delta\phi_{acc}$ of serpentine channel at the stationary energy E_{s1} below

transition energy is

$$
\begin{aligned}
\Delta\phi_{acc} &= \pi - \phi \\
&= \pi - \arccos\left[\frac{V_0 - 2V_{min}}{V_0}\right].
\end{aligned}
\tag{3.26}
$$

As expressed in Eq. 3.26, once ring parameters, i.e. k-value, h, E_{s1} and E_{s2} are fixed, phase acceptance is determined by the peak rf voltage V_0.

As shown in Fig. 3.12, phase acceptance at the stationary energy E_{s1} below the transition energy increases with rf voltage. Phase acceptance at energies different from the stationary energy E_{s1} below the transition energy in the serpentine channel also increases with rf voltage.
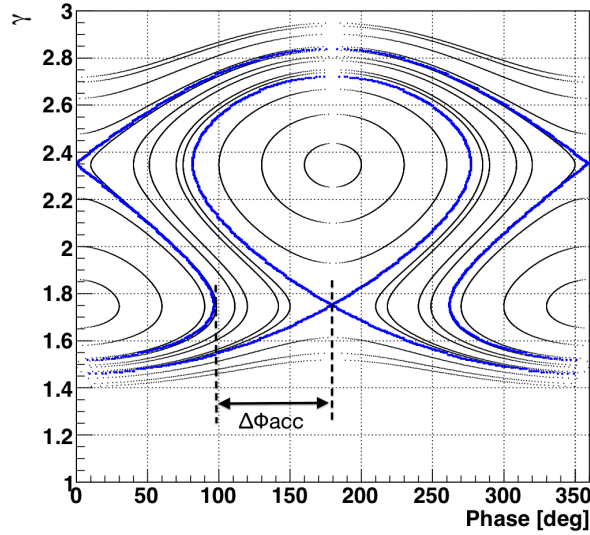
Figure 3.11: Longitudinal phase space with the definition of phase acceptance $\Delta\phi_{acc}$. Blue lines indicate separatrices. The phase acceptance $\Delta\phi_{acc}$ at the stationary energy E_{s1} below the transasition energy is represented here. In this figure, k-value is 3, and the harmonic number h is 1.

Figure 3.12: Phase acceptance $\Delta\phi_{acc}$ at the stationary energy E_{s1} below the transition energy. Radio frequency voltage V_0 is normalized by the minimum rf voltage V_{min}. The minimum rf voltage V_{min} is kept constant while V_0 is increased. In this figure, k-value is 3, and the harmonic number h is 1.

3.5 Serpentine acceleration with square wave rf voltage

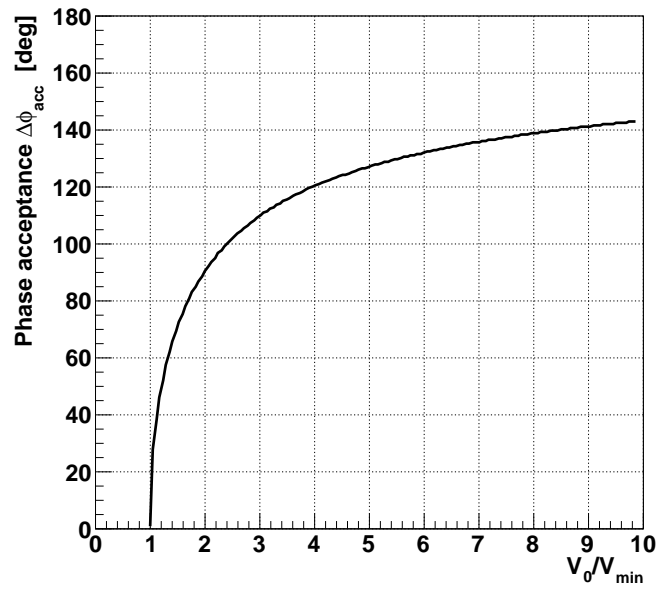The sinusoidal wave rf voltage has been used for modern accelerators. For the serpentine acceleration with sinusoidal wave rf voltage, however, beam energy spread at extraction becomes large. In order to keep mono-energetic beam at extraction, we propose to use square wave rf voltage instead of sinusoidal one for beam acceleration.

The acceleration scheme with square wave rf voltage, so-called flat-top beam acceleration, has been developed in other circular accelerators so far [42, 43, 44, 45, 46]. The square wave rf voltage is generated by a superimposition of Fourier harmonics.

In this section, first the longitudinal hamiltonian with square wave rf voltage is derived analytically in scaling FFAG. Then longitudinal phase space near the transition energy are presented. The energy spread at extraction with square wave rf voltage in serpentine acceleration is evaluated later.

3.5.1 Longitudinal phase space

Using Fourier expansion with rf phase ϕ, we can write an ideal square wave rf voltage at a cavity gap as an infinite series of the form

$$V_{rf} = \frac{4V_0}{\pi} \sum_{n=1}^{\infty} \frac{\sin[(2n-1)\phi]}{2n-1}, \tag{3.27}$$

where V_{rf} is the rf voltage, V_0 is the peak rf voltage, n is the nth harmonics and ϕ is the rf phase.

Now we focus on an infinity harmonics in Eq. 3.27. In this case, the rf voltage V_{rf} can be written as

$$V_{rf} = \begin{cases} V_0 & : -0 < \phi \leqq \pi, \\ -V_0 & : \pi < \phi \leqq 2\pi. \end{cases} \tag{3.28}$$

Then energy equation of motion corresponding to phase ranges can be obtained as follows

$$\frac{dE}{d\Theta} = \begin{cases} \dfrac{eV_0}{2\pi} & : 0 < \phi \leqq \pi, \\[4mm] -\dfrac{eV_0}{2\pi} & : \pi < \phi \leqq 2\pi. \end{cases} \tag{3.29}$$

With the phase equation and energy equation of motion, the longitudinal hamiltonian with square wave rf voltage is derived analytically,

$$H(E, \phi; \Theta) = \begin{cases} h\left[\dfrac{1}{1+\alpha}\dfrac{(E^2 - m^2)^{\frac{1+\alpha}{2}}}{E_s(E_s^2 - m^2)^{\frac{\alpha-1}{2}}} - E\right] - \dfrac{eV_0}{2\pi}\phi & : 0 < \phi \leqq \pi, \\[6mm] h\left[\dfrac{1}{1+\alpha}\dfrac{(E^2 - m^2)^{\frac{1+\alpha}{2}}}{E_s(E_s^2 - m^2)^{\frac{\alpha-1}{2}}} - E\right] + \dfrac{eV_0}{2\pi}\phi - V_0 & : \pi < \phi \leqq 2\pi. \end{cases} \tag{3.30}$$

With the longitudinal hamiltonian written in Eq. 3.30, the longitudinal phase space is shown in Fig. 3.13.

The minimum rf voltage V'_{min} is also derived from Eq. 3.30 as in the same way written in Chapter 3.

$$\begin{aligned} V'_{min} &= 2h\left[\frac{1}{\alpha+1}\left(\frac{P_{s1}^2}{E_{s1}} - \frac{P_{s2}^2}{E_{s2}}\right) + (E_{s2} - E_{s1})\right], \\ &= \frac{2}{\pi}V_{min}, \end{aligned} \tag{3.31}$$

where V_{min} is the minimum rf voltage written in Eq. 3.22 and $E_{s1,s2}$ and $P_{s1,s2}$ are the stationary energies and momenta below and above the transition energy respectively.
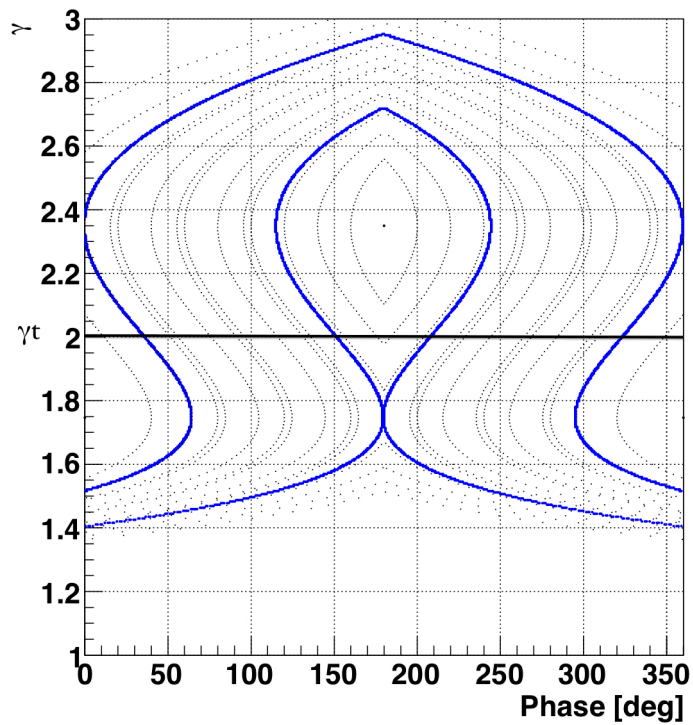
Figure 3.13: An example of longitudinal phase space near the transition energy. Blue lines are separatrices and γ is the Lorenz factor. The transition gamma γ_t is 2 in this figure.

3.5.2   Beam energy spread

To estimate the extraction beam energy spread, longitudinal beam tracking is carried out with stepwise longitudinal beam tracking. As an example, beam trajectories is presented in longitudinal phase space with hamiltonian contour in Fig. 3.14. Longitudinal numerical calculation parameters are summarized in Tab. 3.2. Details of stepwise longitudinal beam tracking can be found in Appendix D.

As shown in Fig. 3.14, with the sinusoidal wave rf voltage, the injected mono-energetic beam has energy spread at extraction. To avoid large energy spread, the phase range of injected beam needs to be narrow when we apply a sinusoidal wave rf voltage in serpentine acceleration. On the other hand, the mono-energetic beam can be obtained at extraction with the square wave rf voltage as shown in Fig. 3.14.
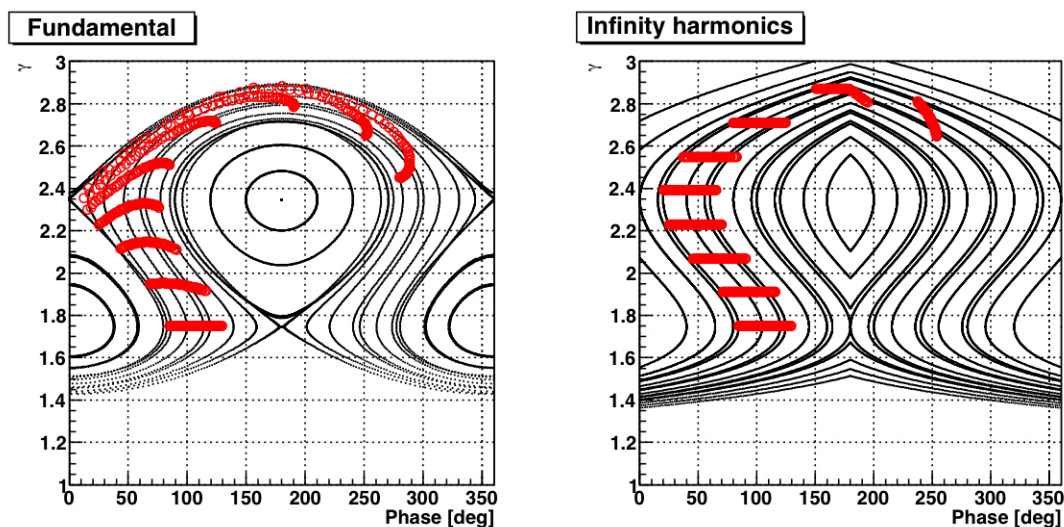
Figure 3.14: Longitudinal phase space with sinusoidal and square wave rf voltage. Red markers indicate the beam trajectories every 10 turns.

Square wave rf voltage is an appropriate rf voltage wave to minimize energy spread after several turns. However, since it is impossible to make an ideal square wave rf voltage, a combination of the fundamental and higher-order harmonic voltages written as Eq. 3.27 are applied in reality. Then, beam energy spread after several turns with square wave rf voltage is studied.

To evaluate beam energy spreads for different sets of harmonics at the extraction energy, stepwise numerical longitudinal beam tracking is carried out. The rf voltages with different sets of harmonics are shown in Fig. 3.15. An example of the longitudinal tracking parameters are written in Tab. 3.2. Examples of injected beam and beam at extraction energy are presented in longitudinal phase space with hamiltonian contours in Fig. 3.16. Energy spread at the extraction energy with different higher-order harmonics are shown in Fig. 3.17.

Table 3.2: Longitudinal parameters for the square wave rf voltage

k-value	3
Mean radius at $\gamma = 1.21$ [m]	5
Transition gamma	2
Stationary gamma below transition	1.75
Injected gamma	1.75
Injected phase range [deg]	85 - 130
Rf voltage [MV/turn]	15 (h=1)
Rf frequency [MHz]	6.5(h=1)

From Fig. 3.17, the higher order harmonics of square wave rf voltage, the smaller beam energy spread can be achieved. It becomes significant from the second order harmonics, where almost 80 % of the beam spread can be suppressed in this case.
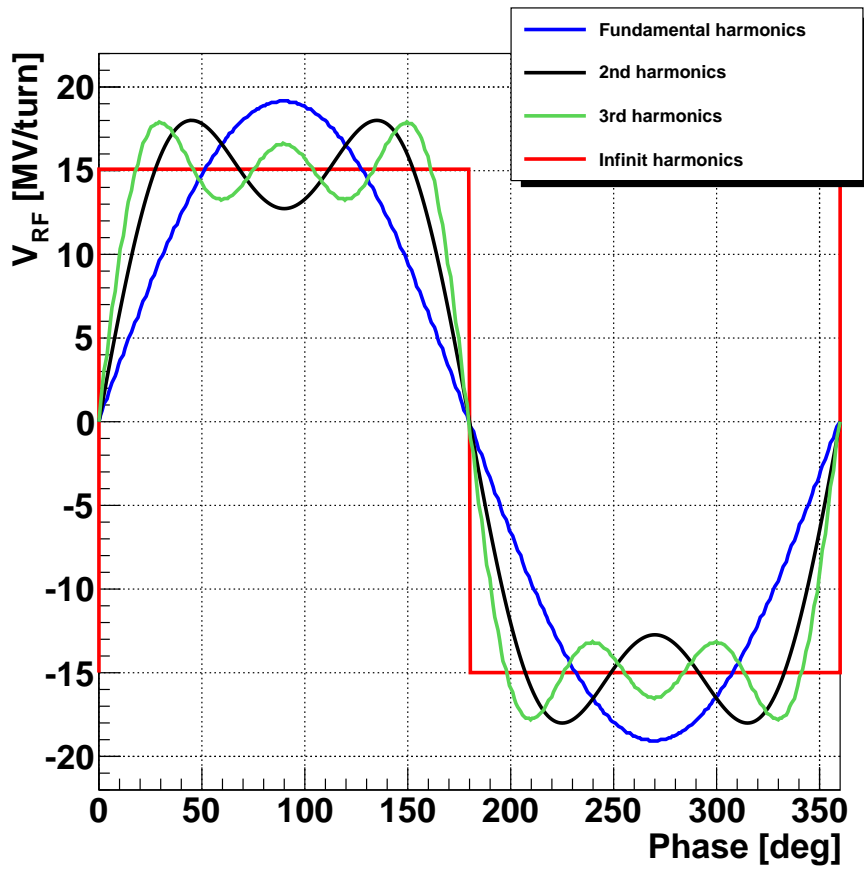
Figure 3.15: Radio frequency voltage wave with different order harmonics. With higher order harmonics, the rf voltage wave becomes square.
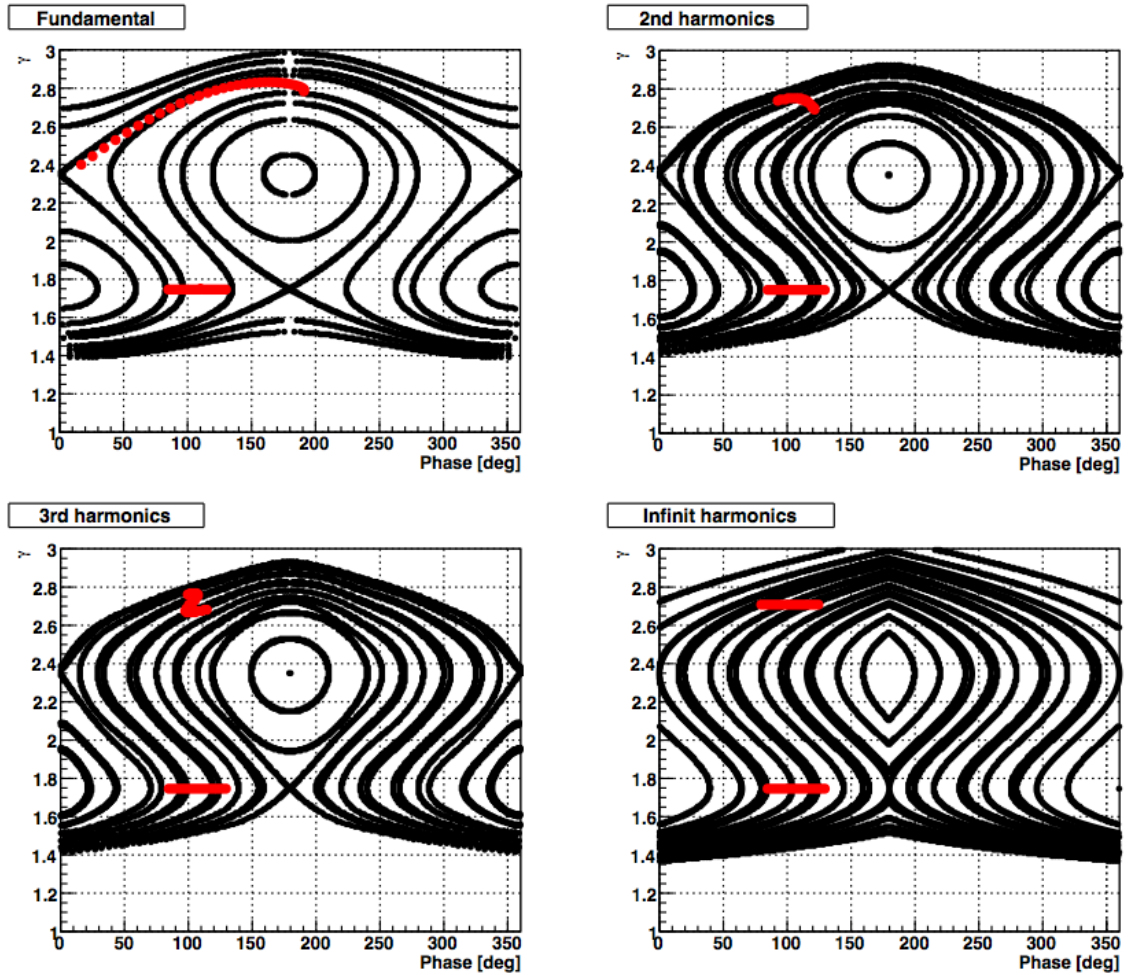
Figure 3.16: Longitudinal phase space with fundamental, third, fifth and infinity harmonics of square wave rf voltage. Stepwise longitudinal tracking results at injection and extraction are indicated by red markers. Phase range of injected beam is from 85 degrees to 130 degrees.
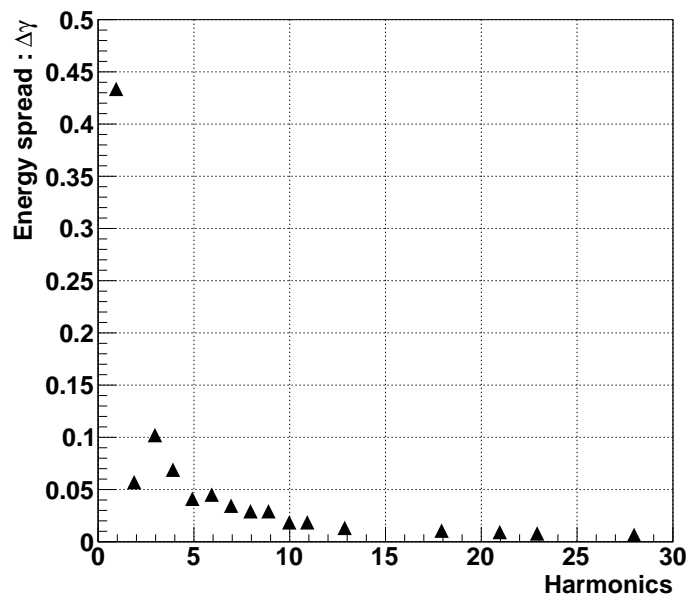
Figure 3.17: Energy spread $\Delta\gamma$ at extraction with different harmonics of square wave rf voltage. In this case, injection phase range is from 85 degrees to 130 degrees. Energy spread $\Delta\gamma$ is determined by the energy deviation between maximum and minimum.

3.5.3 Phase space in non-relativistic energy region with a square rf voltage wave form

If we apply a sinusoidal wave rf voltage, extracted beam has large energy spread, causing beam extraction difficult. One way to avoid this is to inject a beam with small phase range. However it would reduce the beam intensity. On the other hand, if we apply a square wave rf voltage, mono-energetic beam can be extracted. Then we can inject beam in the full phase range of serpentine channel. Furthermore, the phase acceptance of serpentine channel becomes larger than in a sinusoidal wave rf voltage. Therefore, the advantage of using square wave rf voltage in serpentine acceleration is that the high-intensity with mono-energetic beam can be extracted. This acceleration scheme is also achieved in non-relativistic energy region as shown in Fig. 3.18 and Tab. 3.3 as an example.
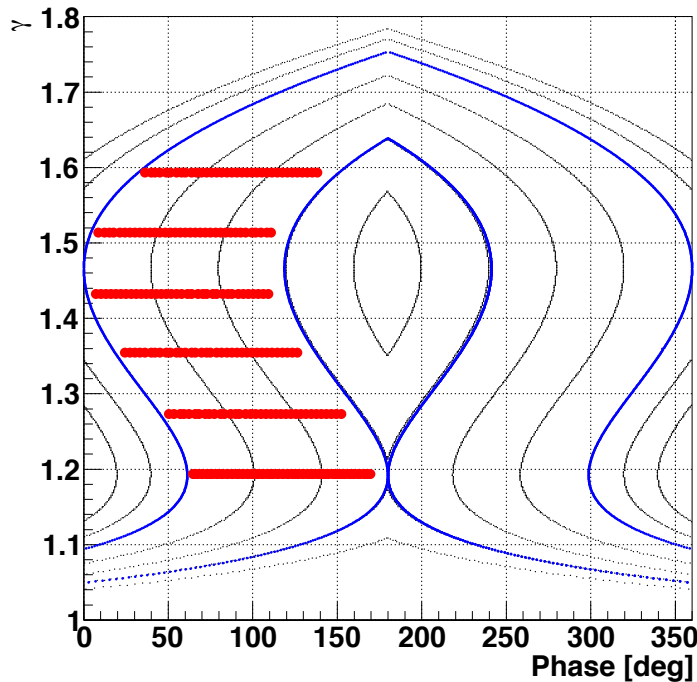
Figure 3.18: Longitudinal phase space in serpentine acceleration with square wave rf voltage. Red lines indicate proton beam every 5 turns.

Table 3.3: Longitudinal parameters for the square rf wave

k-value	0.7
Mean radius at $\gamma = 1.11$ [m]	3
Transition gamma	1.45
Stationary gamma below transition	1.19
Injected gamma	1.19
Injected phase range [deg]	65 - 175
Rf voltage [MV/turn]	15 (h=1)
Rf frequency [MHz]	7.2(h=1)

CHAPTER 4

Experiment

Experimental demonstration of serpentine acceleration in non-scaling FFAG has been done by using the Electron Model for Many Applications, EMMA, at the Daresbury Laboratory in the United Kingdom [33]. Serpentine acceleration in scaling FFAG, however, had not been demonstrated yet. Thus experimental investigation was required to demonstrate it. In this chapter, the features of serpentine acceleration scheme obtained by the experiments are presented [40].

4.1 Experimental apparatus

4.1.1 Overview

Demonstration of serpentine acceleration is done with the electron scaling FFAG ring. The configuration of the ring is shown in Fig. 4.1, and machine parameters are summarized in Tab. 4.1.

Electron beams after the electron gun are accelerated in the acceleration tube up to 160 or 200 keV. Electron beams are injected in the ring by massless septum magnet after passing through the beam shutter and two bending magnets. The electron scaling FFAG ring is designed as a F-D-F triplet radial sector type of scaling FFAG. Radio frequency cavity is a re-entrant cavity with TM_{010} mode (details presented in Appendix B) in the ring. Beams are accelerated at the rf cavity twice per turn. Finally, electron beams are extracted from the ring by the extraction massless septum magnet. Extracted beam energy 8 MeV is measured by using the bending magnet in the extraction beam line.

Since the space to put the rf cavity in the ring is large compared to the drift space at arc sections, the longitudinal hamiltonian with long straight section written in Eq C.4 is used to analyze longitudinal dynamics in this Chapter.

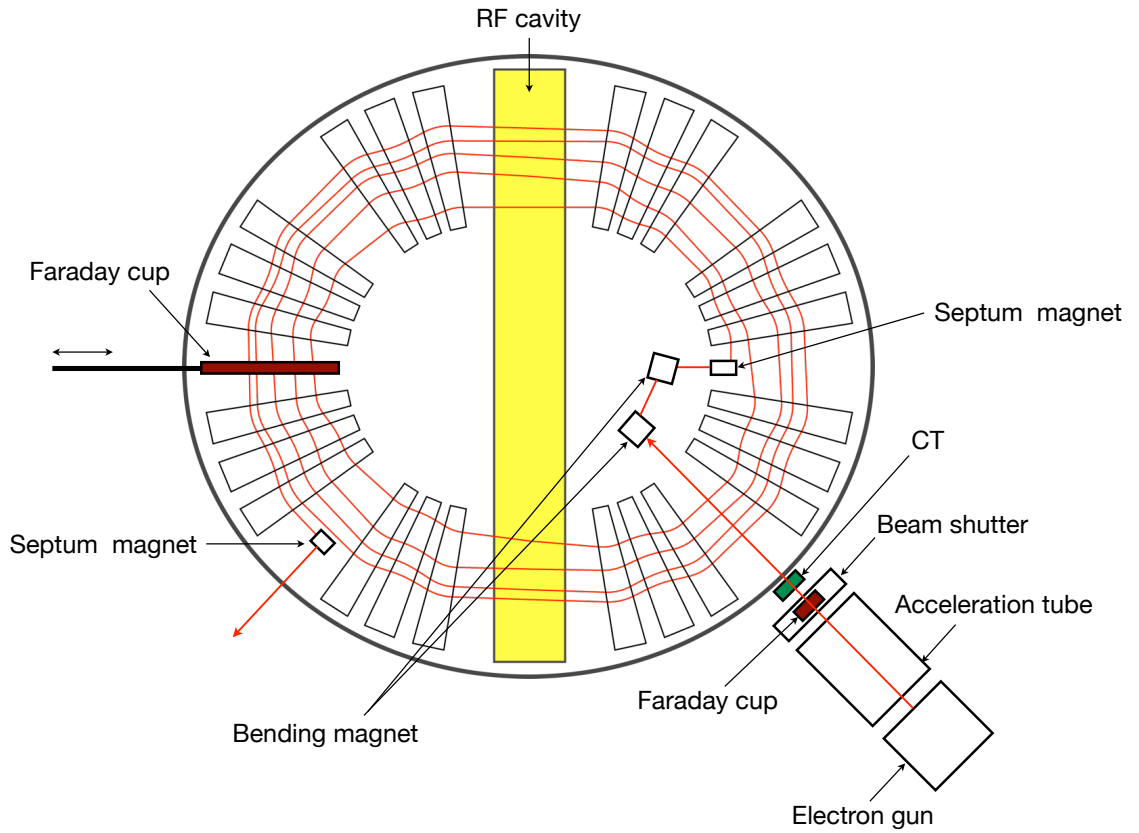Figure 4.1: Schematic view of FFAG ring configuration. The red line indicates the electron beam trajectory.

Table 4.1: Parameter

Particle	Electron
Number of sectors	8
k-value	4.45
Stationary kinetic energy below transition [keV]	205.6
Transition kinetic energy [keV]	764
Total length of long straight sections [m]	0.2
Rf frequency [MHz]	75 (h=1)

4.1.2 Injected electron beam

In order to make a pulsed electron beam, sinusoidal wave rf voltage is applied between cathode and grid electrode as shown in Fig. 4.2. The rf frequency between cathode and grid electrode is equivalent to the rf frequency at the rf cavity in the ring. Bias voltage is also applied at the grid electrode to make a narrow pulsed electron beam. After passing through the grid electrode, electron beam is accelerated from the grid electrode to the anode electrode. Passing through the hole in the anode electrode, electron beam reaches the acceleration tube where it is accelerated up to 160 or 200 keV.
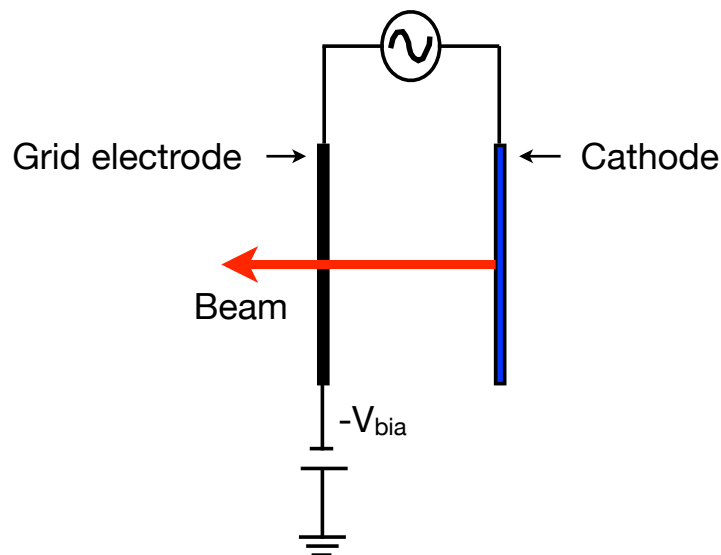
Figure 4.2: Schematic view of cathode and grid electrode in the electron gun.

Beam current from the injector are measured by a Faraday cup made by a copper plate at the beam shutter as represented in Fig. 4.1. The injected electron beam distribution and pulse length in the longitudinal direction are detected by the Current Transformer (CT) just before the ring.

Pulse length of injected beam is less than 20 % of rf period (less than 40 degrees). It means pulse length is less than 3 nsec with 75 MHz rf frequency. Because of this short pulsed beam, it is difficult to estimate exact distribution and pulse length of injected beam with CT.

4.1.3   Beam current and position in the ring

Beam current in the ring are also measured by a Faraday cup made by a
copper plate. Since the Faraday cup is attached on a movable probe, beam
current can be measured from injection to extraction in the ring. If electron
beam is over 600 eV and hits a copper plate, secondary electrons are produced
in the deep part of copper and remain within the internal [47]. Therefore, we
did not prepare a secondary electron suppression system in this experiment.

For the size of a Faraday cup, electron range in material is important. The
range R of particle accelerated to kinetic energy E_{kin} is calculated numerically
from the stopping power [48]. The mechanical size of Faraday cup must be
larger than the electron range in the copper plate.

Beam position in the ring is determined by the tip position of the movable
Faraday cup.

4.1.4   Control system for rf system

Trigger signals from a trigger generator are transmitted to rf generators for
the injector and the amplifier of rf cavity as shown in Fig. 4.3. The rf
frequency applied to the injector and the rf cavity are the same. To control
the initial rf phase at the injector, trigger signal with appropriate delays
comes from the trigger generator. With this system, the initial rf phase into
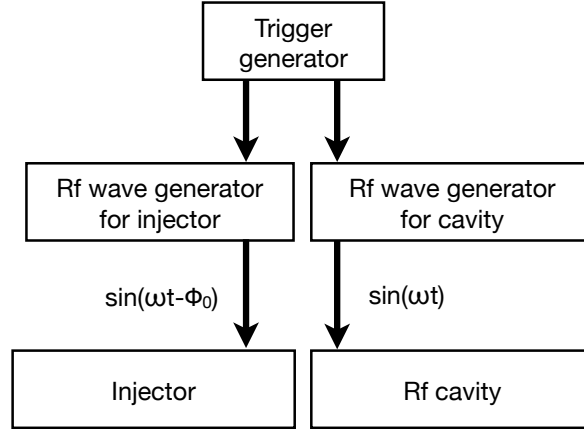the cavity gap can be adjusted.

Figure 4.3: Schematic view of rf control system for injector and rf amplifier. With rf function generator, rf voltage wave $V_0 \sin(\omega t - \phi_0)$ is applied between cathode and grid electrode in the injector, and $V_0 \sin(\omega t)$ is applied the cavity gap. Initial phase at the injector is presented by ϕ_0.

4.2 Measurement

To demonstrate serpentine acceleration, first we measure the electron beam accelerated in serpentine channel. Then phase acceptance of serpentine channel with different rf voltages is measured to clarify the feature of serpentine acceleration.

4.2.1 Demonstration of serpentine acceleration

Longitudinal hamiltonian with fixed rf voltage at 705 kV/gap is presented in Fig. 4.4. The experiment is carried out changing initial rf phase ϕ_0 at the injector. The initial rf phase ϕ_0 is shifted with respect to the rf phase of the rf cavity. Beam current in the ring is measured by the Faraday cup for every initial phases ϕ_0. During measurements, the tip position of the Faraday cup is fixed at 8 MeV orbit. Injected beam energy is fixed at 160 keV.

Injected beam energy is lower than the stationary bucket above the transition energy. Thus, particles cannot be injected in the stationary bucket above the transition energy. Furthermore, beam energy 8 MeV is higher than the stationary energy above the transition energy. Therefore, particles injected in the stationary bucket below the transition energy cannot reach

the Faraday cup fixed at 8 MeV orbit. For these reasons, only particles accelerated in the serpentine channel is measured at the Faraday cup.
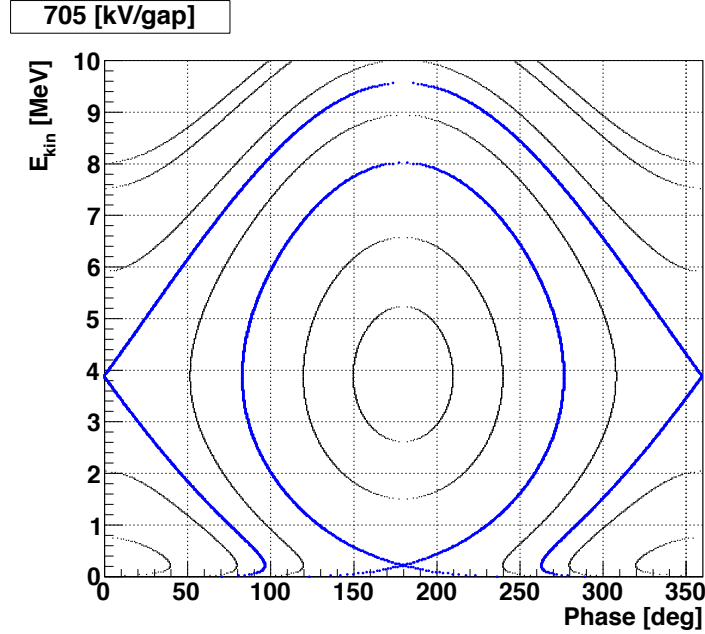
Figure 4.4: Hamiltonian contours in the longitudinal phase space. Blue lines indicate the separatrices.

4.2.2 Experimental result

The experimental results are shown in Fig. 4.5. Error bars of measurement data are estimated by the erratic reading error of beam current $0.015\mu A$ and initial rf phase 5 degrees.

Measurement of the phase range where particles are accelerated with serpentine channel and analytical phase acceptance given by Eq. C.13 are presented in Tab. 4.2. This discrepancy is caused by the fact that injected beam has a phase distribution and a pulse length. However, with the measurement of the phase range where particles were accelerated with serpentine channel, we demonstrate serpentine acceleration in scaling FFAG. The error of measured phase range is estimated by the error propagation with erratic reading error of the initial rf phase.

Figure 4.5: Beam current at the Faraday cup vs initial phase at injector. Blue squares indicate measurement results.

Table 4.2: Phase acceptance

Measurement	Analytical
$120° \pm 7°$	$83°$

4.2.3 Phase acceptance with rf voltage

As discussed in Chapter 3 and shown in Fig. 4.6, the phase acceptance of serpentine channel at injected energy is becoming bigger with rf voltage. To clarify this feature, the experiment consists of five series of data, taken with five different rf voltages.

First, the rf voltage is fixed at 660 kV/gap, and then decreased to 420 kV/gap finally. With the fixed rf voltage, the initial rf phase ϕ_0 at the injector are shifted with respect to the rf phase of the rf cavity. Beam current in the ring is measured with the Faraday cup for every initial phases. Beam current at the Faraday cup in the ring is normalized using the injected beam intensity measured at the beam shutter. The tip position of the Faraday cup is fixed at 8 MeV orbit with different rf voltage. Injected beam energy is fixed at 200 keV.

Beam energy 8 MeV is higher than the stationary energy above the transition energy. Therefore, particles injected in the stationary bucket below the transition energy cannot reach the Faraday cup at 8 MeV orbit. Furthermore, injected beam energy 200 keV is lower than the stationary energy below the transition energy. Thus, particles cannot be injected in the stationary bucket above the transition energy. For these reasons, only particles accelerated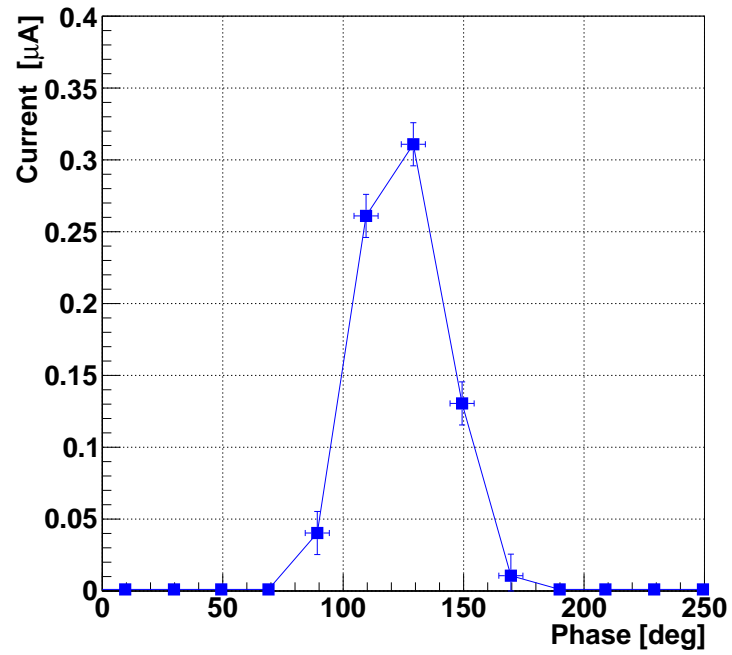 with serpentine channel can be measured at the Faraday cup. Then, changing the initial phase at the injector, we measure the phase acceptance of serpentine channel at injected energy.
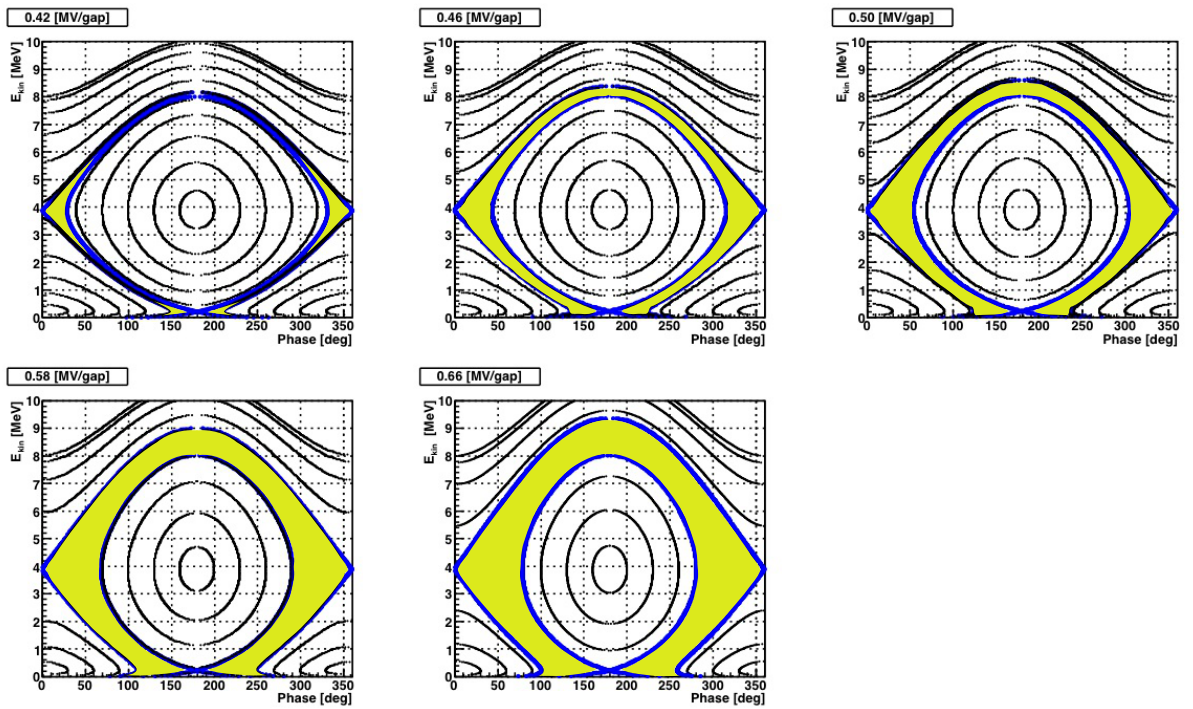
Figure 4.6: Hamiltonian contours in the longitudinal phase space with different rf voltages. Blue lines indicate the separatrices, and yellow parts indicate serpentine channel.

4.2.4   Result analysis for phase acceptance experiment

Accelerating efficiency is given by the beam current at the Faraday cup in the ring normalized using the injected beam intensity at the beam shutter. The experimental results are shown in Fig. 4.7.
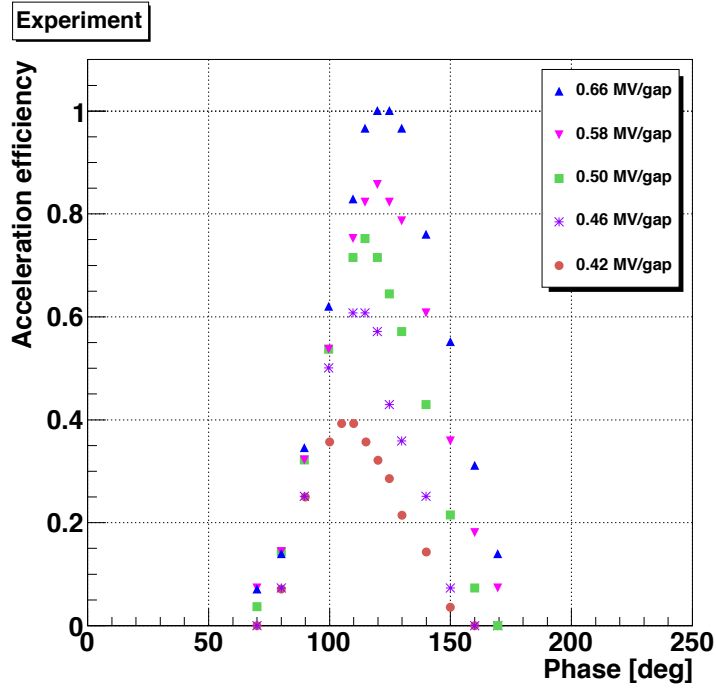
Figure 4.7: Acceleration efficiency Vs rf voltage.

measurement result of phase acceptance

From the acceleration efficiency results shown in Fig. 4.7, the phase acceptance is calculated with the following method.

Phase acceptance are determined by the phase discrepancies at 20% of acceleration efficiency. To determine the phase at 20% of acceleration efficiency, we pick two data points below and above neighborhood of 20% of acceleration efficiency, and linearize the two data points. From the linear function, we obtain the phase at 20% of acceleration efficiency. Analytical phase acceptance are given by Eq. C.13. Measured and analytical phase acceptance with rf voltage are presented in Fig. 4.8. The error bars of mea-

surement data are due to the phase and current errors calculated with error propagation. Details of the error calculation are described in Appendix E.
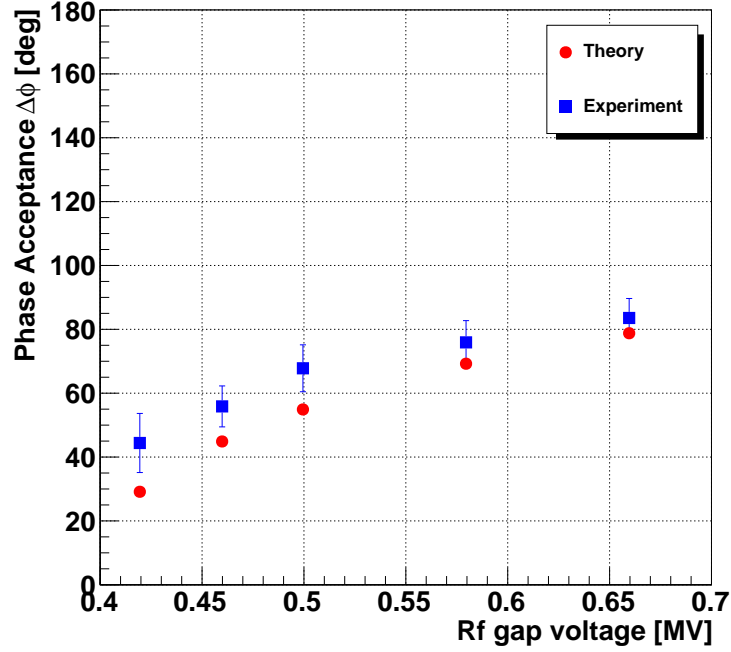
Figure 4.8: Phase acceptance $\Delta\phi$ of serpentine channel with gap rf voltage. Red circles indicate the phase acceptance given by the analytical equation. Blue squares indicate the phase acceptance given by experimental results. The errors of phase and current are estimated to be 5 degrees and $0.15\mu A$ respectively.

As shown in Fig. 4.8, measured phase acceptance becomes bigger with rf voltage. The phase acceptances given by the measurement results are larger than the analytical phase acceptance. These discrepancies are caused by the fact that injected beam has a phase distribution and pulse length. However, the tendency of measurement results are similar to the analytical results.

Summary

In chapter 1, background of this study is presented. Rapid-acceleration schemes and producing high-power beam are required for high-energy accelerators. To realize these requirements, strong focusing, fixed rf acceleration scheme and static magnetic field are necessary conditions. Linear accelerators have been considered as a proper candidate so far. However their cost and power consumption make practical realization difficult. Considering circular accelerators, neither classical cyclotrons nor synchrotrons can be used, since they do not satisfy all the three conditions above. As an alternative candidate, FFAG accelerators have been considered.

Fixed rf frequency acceleration schemes in FFAG accelerators have then been introduced. In scaling FFAGs, a stationary bucket acceleration scheme has been considered so far. A serpentine acceleration scheme has been proposed in non-scaling FFAG. With these acceleration schemes, only relativistic particles are suitable for beam acceleration with fixed rf frequency. However, fixed rf frequency acceleration scheme is also desired in non-relativistic energy region.

The purpose of the study is then presented. To realize fixed rf frequency acceleration not only in relativistic but also in non-relativistic energy region, serpentine acceleration has been introduced in scaling FFAGs. Since energy and phase deviation between synchronous and non-synchronous particles per turn are not small in this case, exact longitudinal dynamics is studied analytically. The aim of this study is to clarify the features of serpentine acceleration scheme in scaling FFAGs, theoretically and experimentally.

In chapter 2, ordinal rf acceleration schemes are studied. If energy and phase deviation between synchronous and non-synchronous particles is small, linearized synchrotron motion is obtained analytically. Phase oscillation and phase stability have been then defined. The features of two types of rf acceleration schemes have been presented. One is frequency-modulated

acceleration scheme, and the other one is fixed frequency acceleration scheme.

In chapter 3, details of a serpentine acceleration scheme in scaling FFAG have been discussed theoretically. In this scheme, since energy and phase deviation of non-synchronous particle per turn are not small, the classical approach of synchrotron motion is not accurate. Then, without linear approximation on the phase and energy variations, the longitudinal dynamics in scaling FFAG with fixed rf frequency is studied. The longitudinal hamiltonian with fixed rf frequency in scaling FFAGs is then derived as follows.

$$H(E, \phi; \Theta) = h\left[\frac{1}{\alpha + 1}\frac{(E^2 - m^2)^{\frac{\alpha+1}{2}}}{E_s(E_s^2 - m^2)^{\frac{\alpha-1}{2}}} - E\right] + \frac{eV_0}{2\pi}\cos\phi,$$

with e charge of the particle, m rest mass, α momentum compaction factor, V_0 rf peak voltage, and the energy variable E canonically conjugate to the coordinate variable ϕ. With this longitudinal hamiltonian, it has been confirmed that serpentine acceleration is possible not only in relativistic but non-relativistic energy region in scaling FFAG.

Features of serpentine acceleration have been presented. First, the minimum rf voltage to realize a serpentine acceleration is examined. The minimum rf voltage is determined by three parameters: k-value, the stationary energy and the rf voltage. The total energy gain of serpentine acceleration has been then studied. The phase acceptance of serpentine channel has also been studied with rf voltage. The total energy gain and the phase acceptance become large with rf voltage.

To extract a narrow energy spread beam from the ring, a square wave rf voltage has been proposed to apply for serpentine acceleration in scaling FFAG. With this acceleration scheme, the longitudinal hamiltonian in scaling FFAG has been derived analytically. Energy spread at extraction energy has been also estimated by a superposition of Fourier harmonics. This method becomes useful to suppress the beam energy spread at extraction.

In chapter 4, the demonstration of serpentine acceleration has been presented with an electron scaling FFAG machine. The apparatus of machine has been presented. To demonstrate the serpentine acceleration in scaling FFAG, the beam accelerated in serpentine channel has been mea-

sured. Then the phase acceptance of serpentine channel has been measured with different rf voltage. The tendency of measured phase acceptance with rf voltage has been similar to analytical phase acceptance.

CHAPTER 6

Discussion and Conclusion

It has been shown that serpentine acceleration in scaling FFAG can be used not only in relativistic energy region but also in non-relativistic energy region, contrary to serpentine acceleration in non-scaling FFAG. The longitudinal hamiltonian with fixed rf frequency scheme has been derived analytically, and minimum rf voltage to make a serpentine channel has been obtained with longitudinal hamiltonian. Total energy gain and phase acceptance of serpentine channel have also been evaluated with rf voltage. The world's first experiment on serpentine acceleration has been conducted with an electron scaling FFAG machine. With the measurement of the beam accelerated in serpentine channel, serpentine acceleration has been validated in scaling FFAGs. We have also confirmed that the tendency of measured phase acceptance with rf voltage has been similar to the analytical phase acceptance.

Now it is interesting to propose a proton FFAG accelerator with serpentine acceleration for ADS.

6.1 Proton driver for ADS

The accelerator for ADS is required to make a proton beam up to several tens of MW power with over 1 GeV beam energy. A low-injected beam energy is also desired. With the study of serpentine acceleration in longitudinal motion so far, small k-value is desired for making lower injected beam energy. Furthermore, small harmonic number are desired for decreasing rf voltage per turn. From these considerations, one of candidates of the longitudinal design for an ADS proton driver is represented in Tab. 6.1 and Fig. 6.1. From Fig. 6.1, 200 MeV proton beam is accelerated over 1 GeV with serpentine channel. In this acceleration scheme, high-intensity proton beam is obtained with c.w. operation.

Table 6.1: Longitudinal parameters for ADS circular proton ring

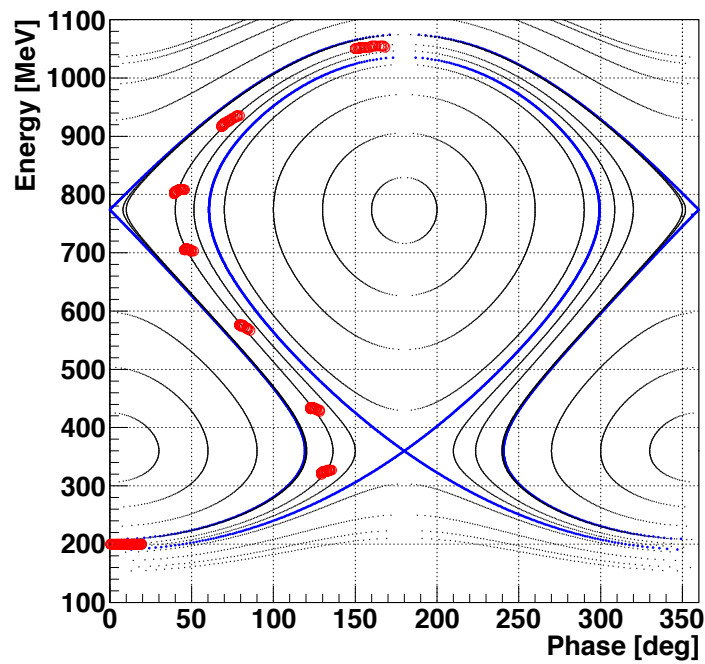|	
k-value	1.45
Equivalent mean radius at 200 MeV [m]	3
Equivalent mean radius at 1 GeV [m]	5.9
Stationary kinetic energy below transition [MeV]	360
rf voltage [MV/turn]	15 (h=1)
rf frequency [MHz]	9.6(h=1)

Figure 6.1: Longitudinal phase space with hamiltonian contours. Red circles indicate beam trajectories every 10 turns. Injected beam energy is 200 MeV and the maximum beam energy is 1.05 GeV. Injection phases are from 0 to 20 degrees. The momentum range from injection to extraction $\Delta P/P_{in}$ is 2.7.

6.2   Further study

Further studies are needed to evaluate more precisely a serpentine acceleration scheme in scaling FFAG.

To make a precise design of scaling FFAG machine with serpentine acceleration, it is mandatory to examine transverse beam dynamics. Furthermore, it is necessary to consider the rf cavity to produce huge rf voltage. Especially for proton driver with serpentine acceleration, several tens of mega volts is needed per turn. The higher total acceleration energy gain is required, the larger rf voltage is needed. Therefore, further detailed technical design of rf cavity to produce huge rf voltage are important issues to make realize a proton driver for ADS with serpentine acceleration in scaling FFAG. Besides, to make a small ring size, detailed technical design of superconducting magnet in scaling FFAG is also necessary.

6.3   Conclusion

The aim of this study was to consider serpentine acceleration in scaling FFAG accelerator. For this purpose, we developed the analytical longitudinal hamiltonian

$$H(E, \phi; \Theta) = h \left[\frac{1}{\alpha + 1} \frac{(E^2 - m^2)^{\frac{\alpha+1}{2}}}{E_s (E_s^2 - m^2)^{\frac{\alpha-1}{2}}} - E \right] + \frac{eV_0}{2\pi} \cos \phi,$$

with fixed rf frequency in scaling FFAG. Using analytical approaches of longitudinal beam dynamics, it has been seen that fixed rf frequency acceleration could be achieved in non-relativistic energy region. With analytical and numerical approaches, it has been also confirmed that the phase acceptance and total energy gain of serpentine channel became bigger with rf voltage.

To demonstrate serpentine acceleration in scaling FFAG practically, world's first beam experiments with electron scaling FFAG machine have been conducted. First, we have measured the beam acceleration in serpentine channel. Then, the phase acceptance of serpentine channel was measured with rf voltage to confirm the feature of serpentine acceleration in scaling FFAG. Finally, from both experiments, serpentine acceleration in

scaling FFAG has been demonstrated practically. This success opens new possibilities for neutrino factory and ADS in the future.

Finally we proposed the longitudinal design of a circular proton ring for ADS with serpentine acceleration in scaling FFAG. Advantage of this ring is that over 1 GeV proton beam with c.w. operation can be obtained. Furthermore, large energy range of beam acceleration can be achieved with only one ring. To realize a proton FFAG ring for ADS practically, we need further technical studies such as rf cavity to produce a huge rf voltage and the super conducting magnet design in scaling FFAG to make a small ring size.

Orbit analysis

First betatron motion around the closed orbit is discussed in this appendix. Then to obtain the magnetic field in scaling FFAG, scaling law is described. Classical approach for the synchrotron motions with linear approximation is discussed later.

A.1 Betatron oscillation

If there is no electric field and only a static magnetic field, the electromagnetic force is written as

$$\vec{F} = e\vec{v} \times \vec{B} = \frac{d}{dt}(\gamma m \vec{v}), \tag{A.1}$$

where e is the charge of particle, γ is the Lorentz factors, m is the rest mass, and v is the particle velocity. In the curvilinear coordinates, we consider the Eq. A.1 with the horizontal axes x as

$$F_x = \frac{d}{dt}(\gamma m \dot{x}) = \gamma m \frac{\beta^2 c^2}{\rho} = -e\beta c B_z, \tag{A.2}$$

and the vertical axes z as

$$F_z = \frac{d}{dt}(\gamma m \dot{z}) = e\beta c B_x, \tag{A.3}$$

where β and γ are Lorentz factor, ρ is the curvature radius of the closed orbit at s, and B_x and B_z are the magnetic field.

Since the deviation of a particle momentum around the closed orbit is assumed very small with respect to d^2x/dt^2 and d^2z/dt^2, we may write

$$\frac{d}{dt}(\gamma m \dot{x}) \simeq \gamma m \left(\ddot{x} - \frac{v^2}{r} \right) = \gamma m (\beta c)^2 \left(\frac{d^2x}{ds^2} - \frac{1}{r} \right), \tag{A.4}$$

where r is the local particle radius. Then Eqs. A.2 and A.3 can be simplified to

$$\frac{d^2x}{ds^2} + \left(\frac{eB_z}{\beta\gamma mc} - 1 \right) r = 0, \tag{A.5}$$

and

$$\frac{d^2z}{ds^2} - \frac{eB_x}{\beta\gamma mc} = 0. \tag{A.6}$$

The local particle radius which is off-momentum closed orbit is written as

$$r = \rho + x. \tag{A.7}$$

By applying the paraxial approximation, i.e.,

$$x, y \ll \rho, r, \tag{A.8}$$

and $p = eB\rho$, Eq. A.5 can be expressed as

$$\frac{d^2x}{ds^2} + \left[\left(1 + \frac{1}{B_0} \frac{\partial B_z}{\partial x} x \right) \left(1 + \frac{x}{\rho} \right) - 1 \right] \rho \left(1 + \frac{x}{\rho} \right) = 0, \tag{A.9}$$

where B_0 is the magnetic field of closed orbit at s. If all terms of second and higher orders in x, z, and their derivatives are neglected in Eq. A.9, the equations of motion in horizontally can be written as

$$\frac{d^2x}{ds^2} + \frac{(1-n)}{\rho^2} x, \tag{A.10}$$

where n called field index is defined as

$$n = -\frac{\rho}{B_0} \left(\frac{\partial B_z}{\partial x} \right)_{x=0}. \tag{A.11}$$

In the vertical plane, Eq. A.6 becomes

$$\frac{d^2z}{ds^2} + \frac{n}{\rho^2} z = 0, \tag{A.12}$$

where Ampere's law $\nabla \times B = 0$ is used:

$$\frac{\partial B_z}{\partial x} = \frac{\partial B_x}{\partial z}. \tag{A.13}$$

Equations A.10 and A.12 are in the form of Hill's equations [49], and also expressed as

$$\frac{d^2y}{ds^2} - K(s)y = 0, \tag{A.14}$$

where y represents either horizontal or vertical displacement, and $K(s)$ satisfies periodic conditions as

$$K(s + C) = K(s), \tag{A.15}$$

where C is the ring circumference of the closed orbit. Then the general solution of Eq. A.14 is

$$y(s) = a\sqrt{\beta(s)} \cos[\phi(s) + \delta], \tag{A.16}$$

with the phase ϕ

$$\phi(s) = \int_0^s \frac{ds}{\beta(s)}, \tag{A.17}$$

where a and δ are constants to be determined by initial conditions, and $\beta(s)$ is the amplitude function of betatron oscillation.

Now we consider that ring circumference satisfies $C = NL$ with N identical superperiods. When the betatron phase advance Φ is given by

$$\Phi = \int_0^L \frac{ds}{\beta(s)}, \tag{A.18}$$

the phase change per revolution is $N\Phi$. The betatron tune ν defined as the number of betatron oscillations in one revolution is

$$\nu = \frac{N}{2\pi} \int_s^{s+L} \frac{ds}{\beta(s)}. \tag{A.19}$$

A.2 Scaling law

We introduce the equivalent radius R of closed orbit defined by

$$R = \frac{1}{2\pi} \oint ds, \tag{A.20}$$

and corresponding equivalent azimuthal angle Θ defined by

$$s = R\Theta, \tag{A.21}$$
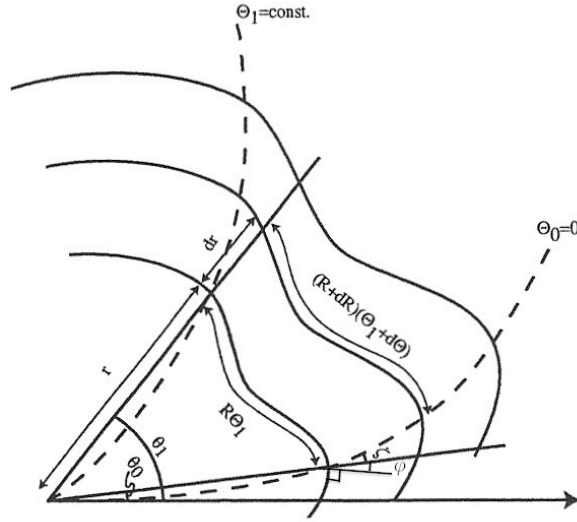
Figure A.1: Schematic view of closed orbit with different momenta in scaling FFAG.

as represented in Fig. A.1.

With Eqs. A.20 and A.21, the linearized equations of motion, i.e. Eqs. A.10 and A.12, can be re-written as

$$
\frac{d^2 x}{d\Theta^2} + \frac{R^2}{\rho^2}(1 - n) \cdot x = 0,
$$

$$
\frac{d^2 z}{d\Theta^2} + \frac{R^2}{\rho^2} n \cdot z = 0.
\tag{A.22}
$$

To have both horizontal and vertical tunes independent of momentum, a necessary and sufficient condition with momentum along the curves $\Theta = const.$ is given by

$$
\left(\frac{\partial (R/\rho)}{\partial p} \right)_{\Theta = const} = 0,
\tag{A.23}
$$

$$
\left(\frac{\partial n}{\partial p} \right)_{\Theta = const} = 0.
\tag{A.24}
$$

Equation A.23 expresses the condition of geometrical similarity of the closed orbits. It implies that the closed orbits for different momenta are all photographic enlargements of each other. Equation A.23 can be also integrated as

$$\rho(p, \Theta) = R(p) \cdot f(\Theta), \tag{A.25}$$

where f is independent of momentum p and determines the shape of the closed orbits. The equivalent radius $R(p)$ shows a scaling factor of closed orbits with different momenta. Equation A.25 is equivalent to:

$$r(p, \Theta) = R(p) \cdot g(\Theta), \tag{A.26}$$

where g is independent of momentum and determines the shape of the closed orbits.

Now we focus on the condition given by Eq. A.24. Equation A.24 expresses the invariance of the field index n with momentum. It means that the focusing forces with different momenta are constant. When we start from the relation

$$p = eB\rho, \tag{A.27}$$

where e is the charge of the particle, the field index n expressed by Eq. A.11 can thus be re-written as

$$n = \left(\frac{\partial \rho}{\partial x}\right) - \frac{\rho}{p}\left(\frac{\partial p}{\partial x}\right). \tag{A.28}$$

In order to transform the coordinate system from (x, s, z) to (R, Θ, z), we use the relation:

$$\frac{\partial}{\partial x} = \left(\frac{\partial R}{\partial x}\right)\left(\frac{\partial}{\partial R}\right)_{\Theta=const.} + \left(\frac{\partial \Theta}{\partial x}\right)\left(\frac{\partial}{\partial \Theta}\right)_{R=const.} \tag{A.29}$$

With Eq. A.29, the field index n with cylindrical coordinate can be described as:

$$n = \left[-\frac{\rho}{R}\left(\frac{R}{p}\frac{dp}{dR} - 1\right)\right] \cdot \left(\frac{\partial R}{\partial x}\right) + \left(\frac{\partial \Theta}{\partial x}\right)R\left(\frac{\partial(\rho/R)}{\partial \Theta}\right)_{R=const.} \tag{A.30}$$

With geometrical considerations [50] and parameters defined in Fig. A.1, field index n can be expressed as:

$$n = -\frac{f(\Theta)}{g(\Theta)}(\cos\varphi + \sin\varphi\tan(\zeta + \varphi))\cdot k + \frac{df}{d\Theta}\tan(\zeta + \varphi), \qquad (A.31)$$

where k called geometrical field index is defined by

$$k = \frac{R}{p}\frac{dp}{dR} - 1. \qquad (A.32)$$

Geometrical similarity gives that the angle φ is independent of momentum along the curves $\Theta = const.$ Then, from Eq. A.31, we can see that if spiral angle ζ and geometrical field index k are independent of momentum, field index n is also independent of momentum. In this case, solving Eq. A.32 , we can get

$$p = p_0\left(\frac{R}{R_0}\right)^{(k+1)}, \qquad (A.33)$$

where R_0 is the equivalent radius regarding to the momentum p_0. Since spiral angle ζ is independent of momentum, the curves $\Theta = const.$ follow logarithmic spirals

$$\theta_{\Theta=const.}(r) = \tan\zeta\cdot\ln\frac{r}{r_0} + \theta_{\Theta=const.(r_0)}. \qquad (A.34)$$

Combining Eqs. A.25, A.27, and A.33, once Eq. A.34 is assumed, the magnetic field distribution in mid-plane also can be expressed in polar coordinate as

$$B(r,\theta) = B_0\left(\frac{r}{r_0}\right)^k\cdot\mathcal{F}\left(\theta - \tan\zeta\cdot\ln\frac{r}{r_0}\right), \qquad (A.35)$$

with function $\mathcal{F}$ independent of momentum p.

A.3 Synchrotron oscillation

The gap voltage V_{rf} of the rf cavity can be expressed as

$$V_{rf} = V_0 \sin \int_0^t \Omega dt = V_0 \sin \phi(t), \qquad (A.36)$$

where Ω is the accelerating angular revolution frequency, and V_0 is the peak voltage. When we assume that the peak rf voltage V_0 and the accelerating angular revolution frequency Ω are slowly-varying functions of time t, or constant, the accelerating angular revolution frequency Ω is written by

$$\Omega = h\Omega_s = \frac{h\beta_s c}{R_s}, \qquad (A.37)$$

where Ω_s is the angular frequency, $\beta_s c$ is the velocity and R_s is the average orbit radius of the synchronous particle, and h is an integer called the harmonic number. A small deviation of momentum Δp_s of synchronous particle is expressed as

$$\Delta p_s = m_0 c \Delta(\beta_s \gamma_s) = \frac{m_0 c}{\beta_s} \Delta \gamma_s = \frac{\Delta E_s}{\Omega_s R_s} \qquad (A.38)$$

where m_0 is the rest mass and c is the light velocity.

The energy gain of synchronous particle in one revolution is given by

$$\delta E_s = eV_0 \sin \phi_s, \qquad (A.39)$$

which, from Eq. A.38, corresponds to a momentum gain δp_s over one turn

$$\delta p_s = \frac{eV_0}{\Omega_s R_s} \sin \phi_s. \qquad (A.40)$$

Now we consider a non-synchronous particle with small deviations of rf parameters from synchronous particle, i.e.

$$\begin{aligned} \Omega = \Omega_s + \Delta\omega, \quad \phi = \phi_s + \Delta\phi, \quad \theta = \theta_s + \Delta\theta, \\ p = p_s + \Delta p, \quad E = E_s + \Delta E. \end{aligned} \qquad (A.41)$$

Here $\Omega_s, \phi_s, \theta_s, p_s, E_s$ are respectively the angular revolution, the synchronous phase angle, the azimuthal orbital angle, the momentum, and the energy of the synchronous particle, and $\Omega, \phi, \theta, p, E$ are the corresponding parameters for an off-momentum particle. Then we have the phase equation

$$\Delta\phi = \phi - \phi_s = -h\Delta\theta, \text{and}$$

$$\Delta\Omega = \frac{d}{dt}(\Delta\theta) = -\frac{1}{h}\frac{d}{dt}(\Delta\phi) = -\frac{1}{h}\frac{d\phi}{dt}. \quad (A.42)$$

The energy gain per revolution for a non-synchronous particle is $eV_0 \sin\phi$, where ϕ is the rf phase angle. Since the revolution time is $2\pi/\Omega$, the average rate of momentum gain per turn of a non-synchronous particle is

$$\dot{p} = \left\langle \frac{dp}{dt} \right\rangle = \frac{eV_0}{2\pi R}\sin\phi, \quad (A.43)$$

where the dot indicates the derivative with respect to time t. With Eq. A.43, the deviation of momentum gain between synchronous particle and non-synchronous particle is thus expressed as

$$R\dot{p} - R_s\dot{p}_s = \Delta(R\dot{p}) = \frac{eV_0}{2\pi}[\sin\phi - \sin\phi_s]. \quad (A.44)$$

Then expanding to the first order,

$$\Delta(R\dot{p}) = R_s\Delta\dot{p} + \dot{p}_s\Delta R + \dots$$

$$= R_s\Delta\dot{p} + \dot{p}_0\left[\left(\frac{dR}{dp}\right)_s\Delta p + \dots\right]$$

$$= R_s\Delta\dot{p} + \left(\frac{dp}{dt}\frac{dR}{dp}\right)_s\Delta p + \dots \quad (A.45)$$

$$= R_s\Delta\dot{p} + \dot{R}_s\Delta p,$$

thus,

$$\Delta(R\dot{p}) = \frac{d}{dt}(R_s\Delta p) = \frac{d}{dt}\left(\frac{\Delta E}{\Omega_s}\right), \quad (A.46)$$

where ΔE is energy deviation between synchronous particle and non-synchronous particle.

In consequence, from Eq. A.44 and A.46, the equation of motion for the energy difference can be written as

$$\frac{d}{dt}\left(\frac{\Delta E}{\Omega_s}\right) = \frac{eV_0}{2\pi}(\sin\phi - \sin\phi_s). \quad (A.47)$$

The dispersion η in revolution frequency called slipage factor is defined as

$$\eta = -\frac{p}{\Omega}\frac{\Delta\Omega}{\Delta p} = \alpha - \frac{1}{\gamma^2}, \qquad (A.48)$$

where $\alpha = 1/\gamma_t^2$ is the momentum compaction factor and γ_t is the transition energy. With Eq. A.42 and A.48, the momentum deviation Δp between synchronous particle and non-synchronous particle is written by

$$\Delta p = -\frac{p_s}{\eta\Omega_s}\Delta\Omega = \frac{p_s}{h\eta\Omega_s}\frac{d\phi}{dt} = \frac{\Delta E}{R_s\Omega_s}, \qquad (A.49)$$

where Δ is a energy deviation of synchronous particle from non-synchronous particle. Thus the phase equation becomes

$$\frac{d\phi}{dt} = \frac{h\eta\Omega_s}{p_sR_s}\left(\frac{\Delta E}{\Omega_s}\right) = \frac{h\eta\Omega_s^2}{\beta_s^2 E_s}\left(\frac{\Delta E}{\Omega_s}\right), \qquad (A.50)$$

where ϕ and $\Delta E/\Omega_s$ are pairs of conjugate phase-space coordinates. Then equations A.47 and A.50 form the synchrotron hamiltonian.

Now we introduce the energy variable W canonically conjugate to the position variable ϕ:

$$W = \frac{\Delta E}{\Omega_s}. \qquad (A.51)$$

The equations of motion A.47 and A.50 can be derived from the Hamiltonian:

$$H(\phi, W) = \frac{h\eta\omega_s^2}{2\beta_s^2 E_s}W^2 + \frac{eV_0}{2\pi}[\cos\phi - \cos\phi_s + (\phi - \phi_s)\sin\phi_s] \qquad (A.52)$$

using the formal rules

$$\dot{\phi} = \frac{d\phi}{dt} = \frac{\partial H}{\partial W} = \frac{h\eta\omega_s^2}{\beta_s^2 E_s}W, \text{and}$$

$$\dot{W} = \frac{dW}{dt} = -\frac{\partial H}{\partial\phi} = \frac{eV_0}{2\pi}[\sin\phi - \sin\phi_s]. \qquad (A.53)$$

APPENDIX B

Radio frequency cavity

Pillbox cavity with TM_{010} mode [51, 52, 53] is considered in this appendix. Relation between rf gap voltage and total power of dissipation is expressed with shunt impedance later.

B.1   Pillbox cavity : TM_{010} mode

Cylindrically symmetric pillbox cavity is the classical type of cavity for beam acceleration. Before considering the details of the pillbox cavity with TM_{010} mode, we find solutions to the wave equations for the magnetic and electric fields using separation of variables.

From Maxwell's equations, the wave equations for the electric field $\vec{E}$ and magnetic field $\vec{H}$ inside the cavity are

$$\nabla^2 \vec{E} + \frac{1}{c}\frac{\partial^2 \vec{E}}{\partial t^2} = 0, \text{and}$$

$$\nabla^2 \vec{H} + \frac{1}{c}\frac{\partial^2 \vec{H}}{\partial t^2} = 0,$$

(B.1)

where c is the speed of light. When we use equations:

$$\vec{E} = \vec{E}\exp(-i\omega t), \text{and}$$
$$\vec{H} = \vec{H}\exp(-i\omega t),$$

(B.2)

and substituting into Eq. B.1, the wave equations satisfy

$$\nabla^2 \vec{E} + k^2 \vec{E} = 0, \text{and}$$
$$\nabla^2 \vec{H} + k^2 \vec{H} = 0,$$

(B.3)

where $k^2 = \omega^2/c^2$ and ω is the angular revolution frequency. The full solutions in cylindrical coordinate (r, ϕ, z) can be derived using the method of

85

separation of variables and boundary conditions. The coordinate z is the longitudinal direction in this case.

The electromagnetic waves in the cavity can be classified into transverse magnetic (TM) mode, for which the longitudinal magnetic field is zero, and transverse electric (TE) mode, for which the longitudinal electric field is zero. From now because we are interested in beam acceleration, let us consider the TM mode in the pillbox cavity of radius a and length l.

Solving Eq. B.3 with the separation of variables method, the components of the electric and magnetic field in the pillbox cavity are given by

$$
\begin{cases}
E_r = -\left(\dfrac{p\pi}{k_c l}\right) E_{mnp} \cdot J\prime_m(k_c r) \cdot \cos(m\phi) \cdot \sin(k_z z) \cdot \exp(-i\omega t), \\[2.5ex]
E_\phi = \left(\dfrac{mp\pi}{k_c^2 r l}\right) E_{mnp} \cdot J_m(k_c r) \cdot \sin(m\phi) \cdot \sin(k_z z) \cdot \exp(-i\omega t), \\[2.5ex]
E_z = E_{mnp} \cdot J_m(k_c r) \cdot \cos(m\phi) \cdot \cos(k_z z) \cdot \exp(-i\omega t), \\[2.5ex]
H_r = -\left(\dfrac{i\omega\epsilon m}{k_c^2 r}\right) E_{mnp} \cdot J_m(k_c r) \cdot \sin(m\phi) \cdot \cos(k_z z) \cdot \exp(-i\omega t), \\[2.5ex]
H_\phi = -\left(\dfrac{i\omega\epsilon}{k_c}\right) E_{mnp} \cdot J\prime_m(k_c r) \cdot \cos(m\phi) \cdot \cos(k_z z) \cdot \exp(-i\omega t), \\[2.5ex]
H_z = 0,
\end{cases}
\tag{B.4}
$$

with the boundary conditions, at $r = a$,

$$
E_\phi = E_z = 0, \tag{B.5}
$$

where $J_m(r)$ is a Bessel function of order m, $J\prime_m(r)$ is the derivative of $J_m(r)$ and ϵ is the dielectric permittivity. The boundary conditions give the radial wave number k_c and the longitudinal wave number k_z;

$$
k_c = \frac{\rho_{mn}}{a},
$$
$$
k_z = \frac{p\pi}{l},
\tag{B.6}
$$

where ρ_{mn} is the nth zero of the mth order Bessel function $J_m(r)$. The resonance wave number k for mode number (m, n, p), m, n, p are integers, is

$$k^2 = k_c^2 + k_z^2. \tag{B.7}$$

Then the resonant frequency of mode TM_{mnp} is given by

$$f_{mnp} = \frac{c}{2\pi}\sqrt{k_c^2 + k_z^2} = \frac{c}{2\pi}\sqrt{\left(\frac{\rho_{mn}}{a}\right)^2 + \left(\frac{\pi p}{l}\right)^2}. \tag{B.8}$$

The lowest resonant frequency acceleration mode in a pillbox cavity is the TM_{010} mode $(m = 0, n = 1, p = 0)$. The fields in the TM_{010} mode are represented as

$$E_z = E_{010}J_0\left(\rho_{01}\frac{r}{a}\right)\cdot\exp(-i\omega t),$$

$$H_\phi = -\left(\frac{i\omega\epsilon}{k_c}E_{010}J\prime_0(k_c r)\cdot\exp(-i\omega t)\right), \tag{B.9}$$

$$E_r = 0, \ E_\phi = 0, \ H_r = 0, \ H_z = 0.$$

Thus the resonant frequency of the TM_{010} mode is determined by the radius of the cavity, and is independent of its length;

$$f_{010} = \frac{c}{2\pi}\frac{\rho_{01}}{a}, \tag{B.10}$$

where $\rho_{01} \sim 2.405$.

B.2 Q value

The walls of the cavity will not be perfectly conducting, and the boundary conditions will vary slightly from those we have assumed. The electric and magnetic fields on the walls will induce currents, which will dissipate the energy. The average rate of energy dissipation $< P_{wall} >$ in the cavity walls is given by

$$< P_{wall} > = \frac{\zeta_m}{2}\int_S |\vec{H}|^2 dS, \tag{B.11}$$

where ζ_m is defined by

$$\zeta_m = \sqrt{\frac{\omega\mu}{2\sigma}}. \tag{B.12}$$

with the electric conductivity σ and the magnetic permeability μ. A useful gauge of the resonator's response to external excitation is the quality factor, or Q-value, given by the ratio of the average stored energy in the cavity to the energy dissipated in the walls during one rf cycle;

$$Q = \frac{\omega W}{< P_{wall} >}. \tag{B.13}$$

where the total energy W stored in the electric field in a cavity is

$$W = \frac{\mu_0}{2} \int_V |\vec{H}|^2 dV. \tag{B.14}$$

In the TM_{010} mode, the Q-value is determined by

$$Q_{010} = \frac{\zeta_0}{2\zeta_m} \cdot \frac{\rho_{01} l}{l + a}. \tag{B.15}$$

B.3   RLC circuit

As a simple example, we substitute the rf cavity with the equivalent RLC parallel resonance circuit as shown in Fig. B.1. The rf gap is equivalent to the capacitance.

The equivalent impedance Z tat the gap as shown in Fig. B.1 is expressed by

$$Z = \frac{i\omega_0 L}{1 - X^2 + i/Q}, \tag{B.16}$$

with

$$\omega_0 = \frac{1}{\sqrt{LC}},$$

$$Q = \frac{R}{\omega_0 L}, \tag{B.17}$$
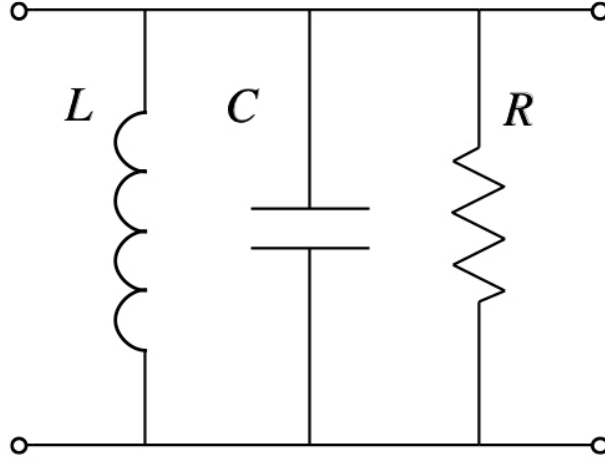
$$X = \frac{\omega}{\omega_0},$$

Figure B.1: RLC parallel resonance circuit of a cavity. The parameter R is the resistance, L is the inductance and C is the capacitance.

where ω_0 is the resonant frequency. At the resonant condition, the shunt impedance R_s is defined by

$$R_s = \frac{V_{eff}^2}{P}, \tag{B.18}$$

with the rf equivalent voltage V_{eff} and the energy dissipation P in the cavity walls. However in accelerator, since we use the rf peak voltage V_{peak} for acceleration, shunt impedance is

$$R_s = \frac{V_{peak}^2}{2P}. \tag{B.19}$$

Substituting Eq B.9 and B.11 into Eq.B.19, the shunt impedance R_s for TM$_{010}$ mode cavity can be written as

$$R_s = \frac{\zeta_0^2}{\zeta_m} \frac{d^2}{\pi J\prime_0^2(\rho_{01}) b(b+l)}, \tag{B.20}$$

with the electric and magnetic field components. Then the inductance L and the capacitance C are derived with shunt impedance as follows;

$$L = \frac{R}{\omega_{010}Q_0},$$
$$C = \frac{Q_0^2}{R\omega_{010}}.$$

(B.21)

From Eq. B.19, once we know the shunt impedance R_s of the cavity, the peak rf voltage V_{peak} at a rf gap can be obtained by the total dissipating energy P in the rf cavity. Furthermore, once material of rf cavity and mode number are decided, the shunt impedance R_s depends only on the geometry of the cavity. For this reason, it is possible to optimize the geometry to achieve the highest shunt impedance.

B.4   High-Q cavity

With Eq. B.16 for RLC parallel resonance circuit, absolute value of impedance $|Z|$ is

$$|Z| = \omega_0 L \sqrt{\frac{1}{(1 - X^2)^2 + (1/Q)^2}}.$$

(B.22)

From Eq. B.22, an impedance with high-Q value ($Q \gg 1$) becomes large and sharp compared to an impedance with low-Q value as shown in Fig. B.2. In this case, when a drive frequency matches with a resonant frequency, rf gap voltage for high-Q cavity is larger than low-Q cavity. However, since a band width of impedance becomes narrow with high-Q cavity, the drive frequency need to be fixed in this case.

In order to vary the shunt impedance during beam acceleration with high-Q cavity, the impedance L and the capacitance C need to be changed temporally. However it is difficult to change a shape of cavity and a distance of rf gap quickly. Because of this reason, mechanically changing of shunt impedance for high-Q cavity cannot be achieved with high repetition rate acceleration scheme.

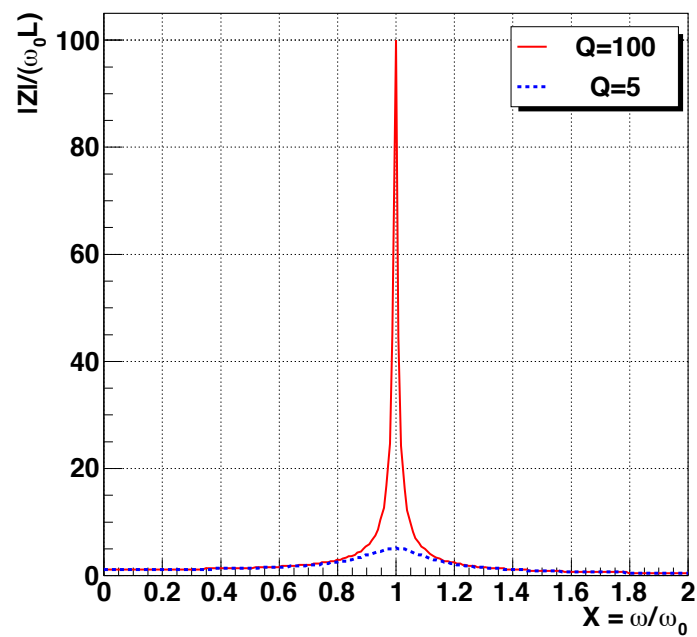For this reason, high-Q cavity is suited for only a fixed rf acceleration scheme.

Figure B.2: Impedance for RLC parallel resonance circuit. Shunt impedance with high-Q value is bigger than low-Q value. With high-Q value, impedance has a narrower band width than low-Q value.

Serpentine acceleration with long straight sections

From the study of serpentine acceleration in longitudinal motion so far, small k-value is required in order to make a injection beam with lower energy. Small harmonic number is also needed for decreasing rf voltage per turn. Since the ring size becomes smaller to satisfy these requirements, inserting long drift spaces to put many rf cavities are considered [39] in this appendix.

C.1 Longitudinal hamiltonian

In order to derive longitudinal hamiltonian, we start from Eq. 3.4. Revolution period of non-synchronous particle T and synchronous particle T_s in a ring with the total length of long straight sections L are related as follows,

$$
\begin{aligned}
\frac{T}{T_s} &= \frac{(2\pi R + L)/\beta c}{(2\pi R_s + L)/\beta_s c} \\
&= \frac{P_s E}{P E_s} \frac{(P/P_s)^A + L/2\pi R_s}{1 + L/2\pi R_s},
\end{aligned}
\tag{C.1}
$$

where $A = \frac{1}{k+1}$, k is the geometrical filed index, R is the equivalent mean radius of the circular part, β is the Lorenz factor, c is the light velocity, and R_s, β_s are the equivalent mean radius and Lorenz factor of the synchronous particle. Combining Eqs. 3.4 and C.1, the phase difference $\Delta\phi$ per turn is

$$
\Delta\phi = 2\pi h \left[\frac{P_s E}{P E_s} \frac{(P/P_s)^A + L/2\pi R_s}{1 + L/2\pi R_s} - 1 \right].
\tag{C.2}
$$

where h is the harmonic number, E_s, P_s, and R_s are the energy, momentum and equivalent mean radius of the synchronous particle. In order to derive the phase and energy equation of motion, $\Delta\phi/2\pi$ is approximated by $d\phi/d\Theta$ as written in Eq. 3.15

$$\frac{d\phi}{d\Theta} = h\left[\frac{P_s E}{P E_s}\frac{(P/P_s)^A + L/2\pi R_s}{1 + L/2\pi R_s} - 1\right], \text{and}$$

(C.3)

$$\frac{dE}{d\Theta} = \frac{eV}{2\pi}\sin\phi,$$

where e is the particle charge. Then longitudinal hamiltonian with long straight section can be derived as

$$H(E,\phi;\Theta) = h\left[\frac{1}{1 + L/2\pi R_s}\frac{\sqrt{E_s^2 - m^2}}{E_s}\cdot\right.$$
$$\left.\left(\frac{1}{1+A}\frac{\sqrt{E^2 - m^2}^{A+1}}{\sqrt{E_s^2 - m^2}^A} + \frac{L}{2\pi R_s}\sqrt{E^2 - m^2}\right) - E\right] + \frac{eV_{rf}}{2\pi}\cos\phi,$$

(C.4)

where we use the convention of the light velocity $c = 1$ in this equation. The equivalent mean radius R_s and the total length of long straight sections L are presented explicitly in Eq. C.4.

C.2   Transition energy

Since long straight sections are in the ring, deviations of the total path length with different momenta do not scale. In this case, the correlation between the momentum deviation ΔP and the deviation of equivalent mean radius ΔR cannot be written as in Eq. 3.11. Thus momentum compaction factor is not determined only by the geometrical field index k, and then transition energy cannot be written as Eq. 3.13. In order to obtain the transition energy with long straight sections in the ring, we start from deriving slippage factor η.

The slippage factor is written by

$$\frac{\Delta T}{T_0} = \eta\frac{\Delta P}{P_0}$$

(C.5)

with the revolution period T and the momentum P, where T_0 and P_0 are the revolution period and the momentum of the synchronous particle, respectively. Assuming that the momentum deviation and revolution period are

small per turn, the slippage factor in the ring with long straight sections can
be written by

$$\eta = \frac{dT}{T_0} \bigg/ \frac{dP}{P_0}.$$ (C.6)

The revolution period T in the ring with long straight sections is presented
as

$$T = \frac{2\pi R + L}{\beta c} = \frac{2\pi R_0 (P/P_0)^{\frac{1}{k+1}} + L}{\beta c}$$ (C.7)

with total length L of straight sections in the ring, the equivalent radius R_0
of the synchronous particle, the geometrical field index k, the Lorentz factor
β and the light speed c. Substituting Eq. C.7 into Eq. C.6, the slippage
factor η is written by

$$\eta = \frac{2\pi R_0}{T_0 P_0^{\frac{1}{k+1}-1}} \frac{P^{\frac{1}{k+1}-2}}{\sqrt{P^2 + m^2}} \left[\frac{1}{k+1}(P^2 + m^2) - m^2 \left(1 + \frac{L}{2\pi R_0} \left(\frac{P_0}{P}\right)^{\frac{1}{k+1}} \right) \right],$$ (C.8)

with the rest mass m and the light speed $c = 1$. Since the transition energy
is the energy at $\eta = 0$, we obtain the transition energy with solving the
equation:

$$\frac{1}{k+1} \left(\frac{P_t^2}{m^2} + 1 \right) - \frac{L}{2\pi R_0} \left(\frac{P_0}{P_t} \right)^{\frac{1}{k+1}} = 1,$$ (C.9)

where P_t is the momentum at the transition energy. Because Eq. C.9 cannot
be solved analytically, numerical calculation is done. The relation between
the transition gamma γ_t and the total length L of straight sections in the
ring is presented in Fig. C.1. From Fig. C.1, the longer the straight sections
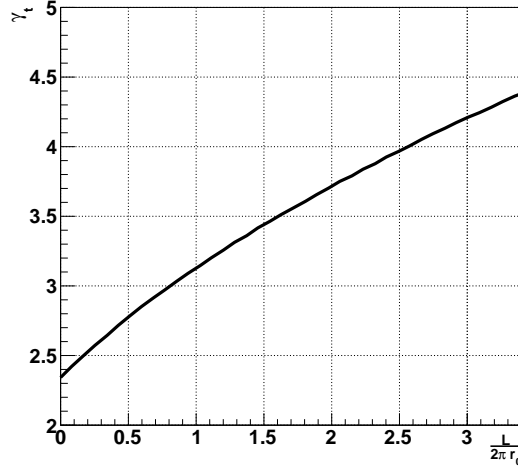are in the ring, the higher the transition energy is.

Figure C.1: Transition energy with the ratio $L/2\pi R_0$.

C.3   Minimum rf voltage to make serpentine channel

In order to derive the minimum rf voltage V_{min} to make a serpentine channel with long straight sections, we start from the condition as following,

$$H(E, \phi; \Theta) = H(E_{s1}, \pi) = H(E_{s2}, 0), \tag{C.10}$$

where E_{s1}, E_{s2} are the stationary energies below and above the transition energy, respectively. From Eqs. C.4 and C.10, the minimum rf voltage V_{min} is derived as

$$V_{min} = \frac{\pi h}{e} \left[\frac{1}{1 + L/2\pi R_{s1}} \frac{P_{s1}}{E_{s1}} \left(\frac{1}{1 + A} \left(P_{s1} - \left(\frac{P_{s2}}{P_{s1}} \right)^A P_{s2} \right) + \frac{L}{2\pi R_{s1}} (P_{s1} - P_{s2}) \right) \right]$$
$$+ \frac{\pi h}{e} (E_{s2} - E_{s1}), \tag{C.11}$$

where e is the particle charge, $A = 1/(k+1)$, k is the geometrical field index, h is the harmonic number, R_{s1} is the equivalent mean radius of the stationary energy below the transition, and the momenta P_{s1}, P_{s2} are the momentum of stationary energies below and above the transition.

The minimum rf voltage V_{min} is related not only to the total length of straight sections but also to the stationary energy difference. Since the transition energy is increased with the total length of straight sections, E_{s2} becomes large when E_{s1} is fixed. In this case, the stationary energy difference is increased as shown in Fig. C.2, and the minimum rf voltage V_{min} is increased as shown in Fig. C.3. On the other hand, if E_{s2} is fixed with the total length of straight sections, E_{s1} is increased. In this case, stationary energy difference is decreased as shown in Fig. C.2, and the minimum rf voltage V_{min} is decreased as shown in Fig C.3.
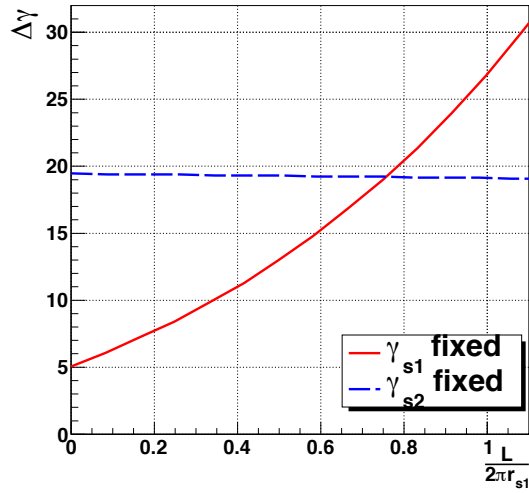

Figure C.2: Stationary energy difference $\Delta\gamma$ defined by $\gamma_{s2} - \gamma_{s1}$ with ratio $L/2\pi r_{s1}$. The Lorentz factors γ_{s1} and γ_{s2} correspond to the E_{s1} and E_{s2} respectively.
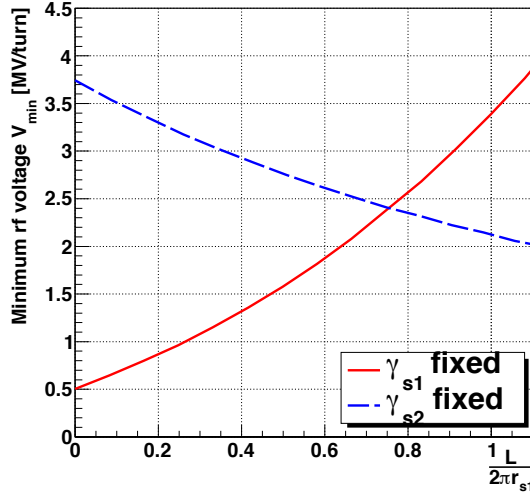
Figure C.3: Minimum rf voltage with ratio $L/2\pi r_{s1}$. The Lorentz factors γ_{s1} and γ_{s2} correspond to the E_{s1} and E_{s2} respectively.

C.4 Phase acceptance

The phase acceptance $\Delta\phi_{acc}$ at the stationary energy E_{s1} below the transition is examined in this section. Since the separatrix which has the point where $H(E_{s1}, \phi)$ passes at the unstable fixed point where $H(E_{s2}, 0)$, $H(E_{s1}, \phi) = H(E_{s2}, 0)$ is obtained. Then the phase ϕ at the E_{s1} is written by

$$\phi = \arccos\left[\frac{2\pi h}{eV_0}\left(\frac{1}{1+L/2\pi R_{s1}}\frac{P_{s1}}{E_{s1}}\left[\frac{1}{1+A}\left(\frac{P_{s2}^{A+1}}{P_{s1}^A} - P_{s1}\right) + \frac{L}{2\pi R_{s1}}(P_{s2} - P_{s1})\right]\right.\right.$$

$$\left.\left. + (E_{s1} - E_{s2})\right) + 1\right],$$

$$= \arccos\left[\frac{V_0 - V_{min}}{V_0}\right],$$

(C.12)

with the minimum rf voltage V_{min} written in Eq. C.11. Therefore, the phase acceptance $\Delta\phi_{acc}$ of serpentine channel with long straight sections at the E_{s1} is

$$\Delta\phi_{acc} = \pi - \phi.$$

(C.13)

C.5 Comparison between race track ring and circular ring

In order to estimate the effect of installing straight sections in a ring, we compare the features of the ring with and without straight sections. Then, the race track ring with two long straight sections in a ring is considered in this section. Furthermore, we decide that the transition energy and the circumference at the transition energy are the same for the circular ring and the racetrack ring.

Since the circumference for the circular ring and the race track ring are the same, we have

$$2\pi R_t = 2\pi r_t + 2l, \tag{C.14}$$

where R_t is the equivalent mean radius for the circular ring at the transition energy, r_t is the equivalent mean radius for the race track ring at the transition energy, and l is the length of one of the two long straight sections. From Eq. C.14, the radius r_t is

$$r_t = R_t - \frac{l}{\pi}. \tag{C.15}$$

Now we set the transition gamma γ_t for circular ring and the transition gamma γ_t' for the race track ring are the same

$$\gamma_t = \sqrt{1 + k_{cir}} = \gamma_t', \tag{C.16}$$

with the k-value of circular ring k_{cir} and the transition gamma γ_t' for the race track ring presented in Eq. C.9.

Note that the transition gamma γ_t' for the race track ring is smaller than the one for the circular ring under the condition where the transition energies are the same for the circular ring and the race track ring. Because of this reason, overall k-value for the race track ring is smaller than the k-value for the circular ring. Thus change in slope of revolution frequency with energy for the race track ring is bigger than the one for circular ring as shown in Fig. C.4.
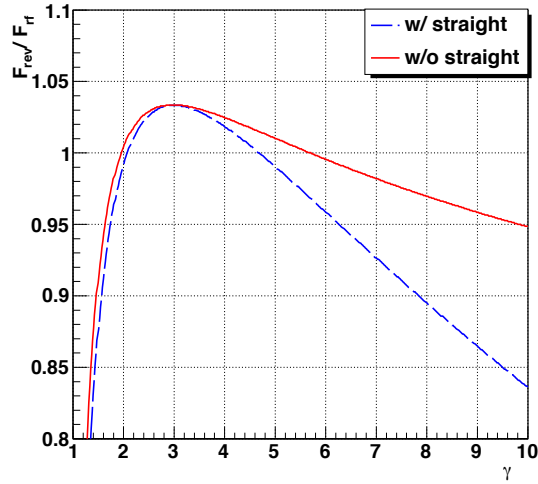
Figure C.4: Normalized revolution frequency and the Lorentz factor γ. Revolution frequency is normalized by the rf frequency. In this case, the total length of straight section $2l$ is 9 times bigger than the circumference of the circular section $2\pi r_t$ at the transition energy. Red line indicates a circular ring case without long straight sections, $l = 0$. Blue doted line indicates racetrack ring case. The energy at $F_{rev}/F_{rf} = 1$ below the transition energy is the stationary energy E_{s1}. Over the transition energy, the energy at the $F_{rev}/F_{rf} = 1$ is the other stationary energy E_{s2}.

C.5.1 Stationary energy deviation and minimum rf voltage

As shown in Fig. C.4, the energy difference between both stationary energies, E_{s1} and E_{s2}, for a racetrack ring becomes smaller than the difference between both stationary energies for the circular ring. Then the minimum rf voltage to make a serpentine channel, expressed in Eq. C.11, for the racetrack ring becomes smaller than for the circular ring. The stationary energy deviations and the minimum rf voltage V_{min} with the ratio $l/\pi r_t$ of the length l of straight section to the circumference πr_t of the arc section in the racetrack ring is shown in Fig. C.5 and C.6.

Therefore, if the transition energy and circumference at the transition energy are the same between the circular ring and the race track ring, difference of both stationary energies is decreased with the length of straight section, and then the minimum rf voltage is decreased.
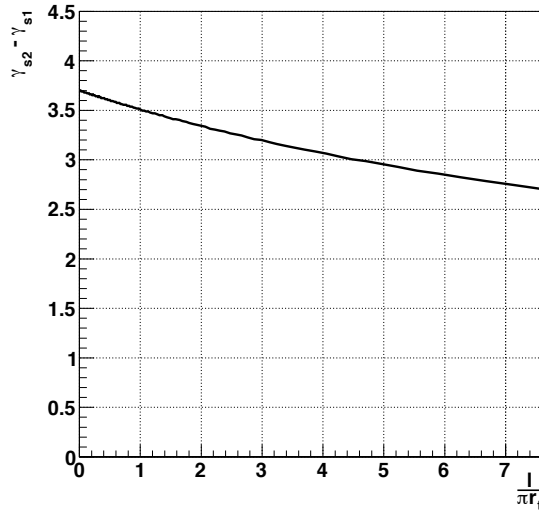

Figure C.5: Stationary energy deviation Vs. the ratio $l/(\pi r_t)$. The radius r_t is the equivalent radius of the racetrack ring at the transition energy and l is the length of one of the two straight sections. The Lorentz factors γ_{s1} and γ_{s2} correspond to E_{s1} and E_{s2}.
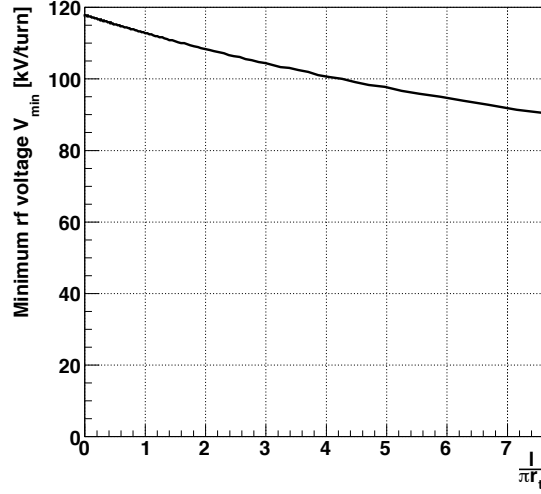
Figure C.6: Minimum rf voltage Vs the ratio $l/(\pi r_t)$. The radius r_t is the radius for a racetrack ring at the transition energy and l is the length of one of the two straight sections. Since stationary energy deviations decreased with length of a straight section, the minimum rf voltage V_{min} becomes smaller.

C.5.2   Phase acceptance and total energy gain

With the constant rf voltage, phase acceptance defined in Fig. 3.11 is examined with variation of the ratio $l/(\pi r_{s1})$ of straight length to circumference of the arc section in the race track ring. Calculation results are presented in Fig. C.7. Since the minimum rf voltage is decreased and the rf voltage is constant with the ratio $l/(\pi r_{s1})$, the phase acceptance of serpentine channel becomes large.

The total energy gain defined by maximum energy E_{max} and minimum energy E_{min} of serpentine channel, shown in Fig. 3.9, is also examined and represented in Fig. C.8.

If the transition energy and the circumference at the transition energy are the same for the circular ring and the racetrack ring, the stationary energy difference is decreased with long straight sections in the ring. Then phase acceptance increased with the length of straight section. On the other hand, since a serpentine channel becomes small with straight sections, the total energy gain is decreased. Therefore, if we want to obtain the same total energy gain with the condition above, bigger rf voltage is needed for the
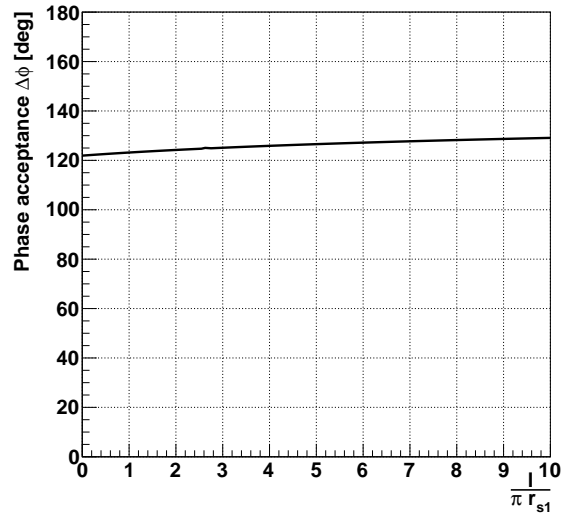
Figure C.7: Phase acceptance at stationary energy below the transition energy E_{s1} Vs. the ratio $l/(\pi r_{s1})$. The equivalent radius r_{s1} is the radius at the stationary energy E_{s1} below the transition energy.

Figure C.8: Total energy gain Vs. ratio $l/(\pi r_{s1})$. The Lorentz factors γ_{max} indicates maximum energy, and γ_{min} indicates minimum energy of serpentine channel. The equivalent mean radius r_{s1} is the energy at the stationary energy E_{s1} below the transition energy.

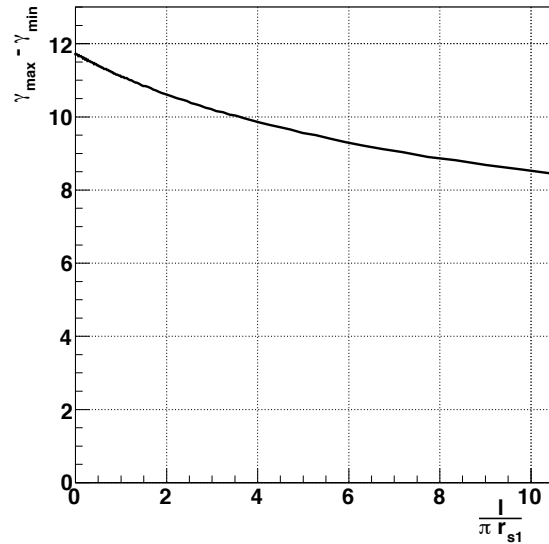racetrack ring compared to the circular ring.

Numerical longitudinal simulation tool

When the longitudinal hamiltonian is derived in Chapter 2, we assume that the energy differences ΔE and phase differences $\Delta \phi$ after passing a cavity is very small. Then $\Delta \phi / 2\pi$ is approximated by $d\phi/d\Theta$. However the energy and phase deviation after passing a cavity is not negligible small in reality. In this case $\Delta \phi / 2\pi$ cannot be approximated by $d\phi/d\Theta$. Thus the differential equations for beam tracking are introduced in longitudinal motion.

Since a particle gains energy from rf cavity, the velocity and circumference of a particle is changed. Time of flight can be calculated with the velocity and circumference. Particle phase after passing a cavity is then calculated with the time of flight and rf frequency. In this procedure, the canonical equations can be expressed as

$$E_{i+1}(E_i, \phi_i) = E_i + g(\phi_i) \tag{D.1}$$

$$\phi_{i+1}(E_{i+1}, \phi_i) = \phi_i + 2\pi f_{rf}\left(\frac{2\pi R_{i+1}}{\beta_{i+1}}\right), \tag{D.2}$$

where E and ϕ are the canonically conjugate values, f_{rf} is the rf frequency, E_i and ϕ_i are their parameters after passing the ith cavity, E_{i+1}, ϕ_{i+1}, R_{i+1} and β_{i+1} are their parameters after passing the $i+i$th cavity, and $g(\phi_i)$ is $eV_{rf}\sin(\phi_i)$.

In order to clarify that the beam acceleration for many turns is stable in longitudinal phase space, it is necessary for Eqs. D.1 and D.2 to satisfy the symplectic condition [54, 55].

Equation D.2 is rewritten with Eq. 3.9 and Eq. D.1 as

$$\phi_{i+1}(E_{i+1}, \phi_i) = \phi_i + 4\pi^2 f_{rf}\frac{R_0}{P_0^\alpha}E_{i+1}P_{i+1}^{\alpha-1}, \tag{D.3}$$

where $\alpha = 1/(k+1)$, and the second term of the Eq. D.3 is replaced by $f(E_{i+1})$. Then the differential equation of energy and phase is expressed by

$$\phi_{i+1}(E_{i+1}, \phi_i) = \phi_i + f(E_{i+1}) \tag{D.4}$$

We assume that the Jacobian matrix S is expressed by Eq. D.1 and Eq. D.2. The symplectic condition is then derived by

$$S^T J S = J, \tag{D.5}$$

where J is a matrix written by

$$J = \begin{pmatrix} 0 & -1 \\ 1 & 0 \end{pmatrix}.$$

If the differential equations are satisfied with symplectic condition, the Jacobian $|S|$ becomes 1.

The Jacobian matrix S is written by

$$S = \begin{pmatrix} \frac{\partial E_{i+1}}{\partial E_i} & \frac{\partial E_{i+1}}{\partial \phi_i} \\ \frac{\partial \phi_{i+1}}{\partial E_i} & \frac{d\phi_{i+1}}{d\phi_i} \end{pmatrix},$$

then each element of matrix are calculated as

$$S_{11} = \frac{\partial E_{i+1}}{\partial E_i} = 1 \tag{D.6}$$

$$S_{12} = \frac{\partial E_{i+1}}{\partial \phi_i} = \frac{dg}{d\phi_i} \tag{D.7}$$

$$S_{21} = \frac{\partial \phi_{i+1}}{\partial E_i} = \frac{\partial f}{\partial E_i} \tag{D.8}$$

$$S_{22} = \frac{\partial \phi_{i+1}}{\partial \phi_i} = 1 + \frac{\partial f}{\partial \phi_i}. \tag{D.9}$$

Finally the Jacobian $|S|$ is expressed as

$$\begin{aligned} |S| &= 1 + \frac{\partial f}{\partial \phi_i} - \frac{dg}{d\phi_i}\frac{\partial f}{\partial E_i} \\ &= 1 + \frac{\partial f}{\partial E_{i+1}}\frac{\partial E_{i+1}}{\partial \phi_i} - \frac{dg}{d\phi_i}\frac{\partial f}{\partial E_i} \\ &= 1 + \frac{\partial f}{\partial E_{i+1}}\frac{\partial E_{i+1}}{\partial \phi_i} - \frac{\partial E_{i+1}}{\partial \phi_i}\frac{\partial f}{\partial E_{i+1}}\frac{\partial E_{i+1}}{\partial E_i} \\ &= 1. \end{aligned} \tag{D.10}$$

Therefore, the differential equations in longitudinal motion are satisfied with symplectic condition. Beam motions in longitudinal phase space are calculated by following equations;

$$E_{i+1} = E_i + V_{RF}\sin(2\pi F_{RF}T_i) \tag{D.11}$$

$$P_{i+1} = \beta_{i+1}E_{i+1} \tag{D.12}$$

$$R_{i+1} = R_0\left(\frac{P_{i+1}}{P_0}\right)^{\frac{1}{k+1}} \tag{D.13}$$

$$L_{i+1} = 2\pi R_{i+1}$$

$$T_{i+1} = T_i + \frac{L_{i+1}}{\beta_{i+1}} \tag{D.14}$$

where E_i, P_i, R_i, L_i and T_i are the parameters after passing the ith rf cavity, and E_{i+1}, P_{i+1}, R_{i+1}, L_{i+1} and T_{i+1} are the parameters after passing the $i + 1$th rf cavity.

Details of the calculation for error estimation using the propagation method

In Chapter 4, phase acceptance $\Delta\phi$ is simply estimated by the phase difference at 20 % of acceleration efficiency. To obtain phase at 20 % of acceleration efficiency, we pick up two data below and above neighborhood 20 % of acceleration efficiency, and linearize the two data. Then phase acceptance $\Delta\phi$ is written as

$$\Delta\phi = \phi_{max} - \phi_{min}, \tag{E.1}$$

with edges of phase acceptance ϕ_{min} and ϕ_{max} defined in Fig. E.1.
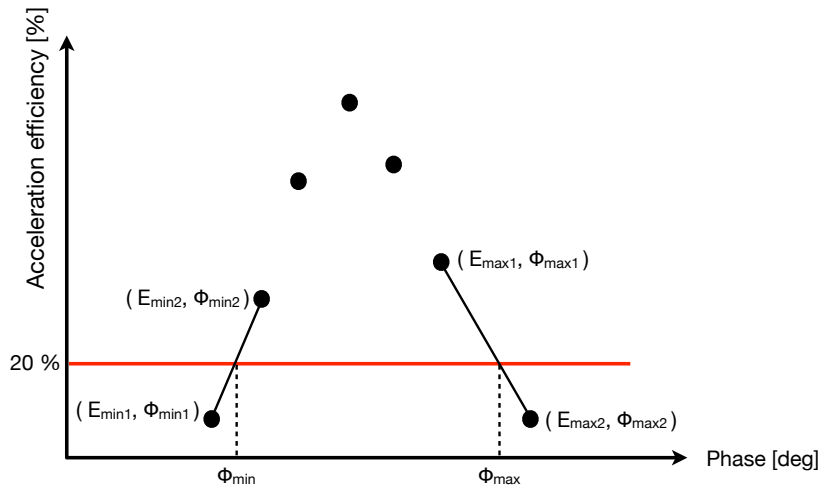
Figure E.1: The schematic drawing of acceleration efficiency and initial rf phase. Black dots indicate measured data.

Error of phase acceptance $\sigma_{\Delta\phi}$ is calculated by

$$\sigma_{\Delta\phi} = \sqrt{\sigma_{\phi_{max}}^2 + \sigma_{\phi_{min}}^2}. \tag{E.2}$$

The maximum phase ϕ_{max} and the minimum phase ϕ_{min} of phase acceptance replaced by ϕ_m are obtained as following equation:

$$\phi_m = \frac{0.2 - b}{a}, \tag{E.3}$$

where a is the slope written by

$$a = \frac{E_2 - E_1}{\phi_2 - \phi_1}, \tag{E.4}$$

and b is the intercept of the linear function expressed as

$$b = E_2 - a \cdot \phi_2$$
$$= E_1 - a \cdot \phi_1, \tag{E.5}$$

where the E_1 indicates E_{min1} and E_{max1} and the ϕ_1 indicates ϕ_{min1} and ϕ_{max1} respectively. The efficiency E_2 and the phase ϕ_2 are defined by the same way as the energy E_1 and the phase ϕ_1.

Applying Eqs. E.4 and E.5 into the Eq. E.3, the edges of phase acceptance ϕ_m can be expressed as

$$\phi_m = \frac{0.2 - (E_1 - a \cdot \phi_1)}{(E_2 - E_1)/(\phi_2 - \phi_1)}$$
$$= \frac{(0.2 - E_1) \cdot \phi_2 + (E_2 - 0.2) \cdot \phi_1}{E_2 - E_1}. \tag{E.6}$$

From Eq. E.6, we get

$$\frac{\partial \phi_m}{\partial \phi_1} = \frac{E_2 - 0.2}{E_2 - E_1},$$

$$\frac{\partial \phi_m}{\partial \phi_2} = \frac{0.2 - E_1}{E_2 - E_1},$$

$$\frac{\partial \phi_m}{\partial E_1} = \frac{(0.2 - E_2) \cdot \phi_2 + (E_2 - 0.2) \cdot \phi_1}{(E_2 - E_1)^2},$$ (E.7)

$$\frac{\partial \phi_m}{\partial E_2} = \frac{(0.2 - E_1) \cdot \phi_1 - (0.2 - E_1) \cdot \phi_2}{(E_2 - E_1)^2}.$$

Using these formulas, the errors σ_{ϕ_m} for edges of phase acceptance can be calculated as

$$\sigma_{\phi_m}^2 = \left(\frac{\partial \phi_m}{\partial E_1}\right)^2 \sigma_{E1}^2 + \left(\frac{\partial \phi_m}{\partial E_2}\right)^2 \sigma_{E2}^2 + \left(\frac{\partial \phi_m}{\partial \phi_1}\right)^2 \sigma_{\phi_1}^2 + \left(\frac{\partial \phi_m}{\partial \phi_2}\right)^2 \sigma_{\phi_2}^2,$$ (E.8)

where σ_{E1}, σ_{E2}, σ_{ϕ_1} and σ_{ϕ_2} indicate the error of efficiency and phase at points respectively. To obtain errors of the efficiency σ_{E1} and σ_{E2}, we start from the acceleration efficiency E defined by

$$E = \frac{I_{8MeV}}{I_{Inj}},$$ (E.9)

where I_{8MeV} indicates the beam current at 8 MeV closed orbit and I_{inj} indicates the injection beam current. Thus errors of efficiency σ_{E1} and σ_{E2} replaced by σ_E is written by

$$\sigma_E^2 = \left(\frac{\partial E}{\partial I_{inj}}\right)^2 \sigma_{I_{inj}}^2 + \left(\frac{\partial E}{\partial I_{8MeV}}\right)^2 \sigma_{I_{8MeV}}^2.$$ (E.10)

Substituting the Eqs. E.8 and E.10 into the Eq. E.2, the error for the phase acceptance $\sigma_{\Delta \phi}$ is calculated.

Bibliography

[1] S. Geer, Muon Colliders and Neutrino Factories, Annual Review of Nuclear and Particle Science, Vol.59, p.347-365, (2009).

[2] S. Geer, Neutrino beams from muon storage rings: Characteristics and physics potential, Phys. Rev. D 57 (11), p. 6989-6997 (1998).

[3] K. Mishima, et al., Journal of Nuclear Science and Technology, vol.44, NO3 Special Issue on Global 2005, p.499-503, (2007).

[4] A. C. Mueller, Prospect for transmutation of nuclear waste and associated proton-accelerator technology, The European Physical Journal, vol.176, pp. 179-19, (2009).

[5] S. Machida, Space charge effect, OHO 2000, (2000).

[6] S. Nagamiya, Over view of J-PARC, Lecture Notes in Physics, vol.781, p. 1-16, (2010).

[7] S. Y. Lee, A Multipole Expansion for the field of Vacuum Chamber Eddy Currents, Nucl. Instr. and Meth. A 300, p.151-158, (1991).

[8] E. D. Courant and H.S. Snyder, Theory of the Alternating-Gradient Synchrotron, Annals of Physics: 3, p. 1-48, (1958).

[9] S. D. Holmes, Project X -Reference Design Report, V1.0 November 1, 2010, URL http://projectx.fnal.gov/index.shtml.

[10] A. A. Kolomensky, V. A. Petukhov and M. S. Rabinovich, Some problems in the theory of cyclic accelerators, Academy of Sciences of the USSR, Moscow, p. 7, (1955).

[11] K. R. Symon, D. W. Kerest, L. W. Jones, L. J. Laslett, and K. M. Terwillinger, Fixed-field alternating-gradient particle accelerators, Physical Review, Vol.103, No.6, p. 1837-1859, (1956).

[12] T. Ohkawa, Symposium on Nuclear Physics of Japan Physics Society, (1953).

[13] K. R. Symon and A.M. Sessler, Methods of radio frequency acceleration in fixed field accelerators with applications to high current and intersecting beam accelerators, CERN symposium, p. 44-62, (1956).

[14] D. W. Kerst, et al., Fixed field alternating gradient accelerators with spirally ridged poles, Phys. Rev. 98 (4) (1955) 1153, in: Minutes of the Meeting of the Division of Fluid Dynamics, Virginia, November, p. 1153, (1954).

[15] D. W. Kerst, E.A. Day, H. J. Hausman, R. O. Haxby, L. J. Laslett, F.E. Mills, T. Okawa, F. L. Peterson, E. M. Rowe, A. M. Sessler, J. N. Snyder, and W. A. Wallenmeyer, Electron model of a spiral sector accelerator, Rev. Sci. Instrum. 31 (10), p. 1076-1106, (1960).

[16] F. T. Cole, G. Parzen, C. H. Pruett, W. A. Wallenmeyer, and D. E. Young, MURA 50-MeV electron accelerator general description and review, Rev. Sci. Insturm. Vol. 35, No.11, p. 1393-1397, (1964).

[17] F. T. Cole et al., Electron Model Fixed Field Alternation Gradient Accelerator, Rev. Sci. Instrum. Vol.28, No.6, p. 403, (1957).

[18] Y. Mori et al., A new type of rf cavity for high intensity proton synchrotron using high permeability magnetic alloy, Proc. of EPAC '98, p. 299, (1998).

[19] M. Aiba et al., Development of a FFAG proton synchrotron, Proc. of EPAC '00, p. 581-583, (2000).

[20] Y. Ishi, et. al,. PRESENT STATUS AND FUTURE OF FFAGS AT KURRI AND THE FIRST ADSR EXPERIMENT, Proc. of IPAC '10, (2010).

[21] C. H. Pyeon, et al., First injection of spallation neutrons generated by high-energy protons into the Kyoto University Critical Assembly, J. Nucl. Sci. Tech. 46 (12), 1091-1093, (2009).

[22] K. Yoshimura, Prism overview, Nucl. Instr. and Meth. A 503 (1-2), 254-257, (2003).

[23] Y. Kuno, Muon Particle and Nuclear Physics Programs at J-PARC, Lect. Notes Phys. 781, pp.231-262, (2009).

[24] Y. Mori, et. al., A Letter of Intent to The J-PARC 50 GeV Proton Synchrotron Experiments, The PRISM Project - A muon Source of the World-Highest Brightness by Phase Rotation-, (2003).

[25] Y. Kuriyama, "Development of a New Method To Evaluate Performance of Accelerator Magnets by Transporting Alpha Particles", Ph.D Thesis, Department of Physics, Osaka University (2008).

[26] Y. Mori, Development of FFAG accelerators and their applications for intense secondary particle production, Nucl. Instr. and Meth. A 562 (2), p. 591-595, (2006).

[27] K. Okabe, et al., RECENT STUDY OF THE FFAG-ERIT SYSTEM FOR BNCT, Proc. of PAC'09, FR5REP115, (2009).

[28] T. Planche, et al., Scaling FFAG rings for rapid acceleration of muon beams, Nucl. Instr. and Meth. A, Vol. 622 (1), p. 21-27, (2010).

[29] T. Planche, et al., Harmonic number jump acceleration of muon beams in zero-chromatic FFAG rings, Nucl. Instr. and Meth. A, Vol. 632 (1), p. 7-17, (2011).

[30] S. Koscieniak, et al., Longitudinal Dynamics in an FFAG Accelerator Under Conditions of Radio Acceleration and Fixed, High RF, IEEE Particle Accelerator Conf. Portland OR., May 12-16, p. 1831, (2003).

[31] S. Koscielniak, et al., Mechanisms for Nonlinear Acceleration in FFAGs with Fixed RF, Nucl. Instr. and Meth. A, Vol.523, Issues 1-2, p. 25-49, 01, May 2004.

[32] B. Barlow, et al., EMMA-The world's first non-scaling FFAG, Nucl. Instr. and Meth. A, Vol. 624 (1), p. 1-19, (2010).

[33] S. Machida, et al., Acceleration in the linear non-scaling fixed-field alternating-gradient accelerator EMMA, Nature Physics, Vol.8, No.3, p. 243-247 (2012).

[34] E. Yamakawa , T.Uesugi and Y.Mori, Stationary Bucket Acceleration in the Scaling FFAG Accelerator, International Journal of Modern Physics A, Vol.26, p. 1685-1872, (2011).

[35] Y. Mori, FFAG accelerators and their applications, Proc. of EPAC 06 Conference, Edinburgh, UK, pp. 950-954, (2006).

[36] T. Planche, Study of zero-chromatic FFAG synchrotron for muon acceleration, Ph.D Thesis, Graduate School of Engineering, Kyoto University (2010).

[37] E. Yamakawa, T. Planche, J.-B Lagrange, T. Uesugi, Y. Kuriyama, Y. Ishi, Y. Mori, I. Sakai, K. Okabe, M. Inoue, THE STUDY OF NEW TYPE OF RF ACCELERATION IN SCALING FFAG ACCELERATION, 7th Annual Meeting of Particle Accelerator Society of Japan, p. 450-452, (2010).

[38] E. Yamakawa, J-B. Lagrange, R. Nakano, Y.Ishi, T. Uesugi, Y. Kuriyama, B. Qin, K.Okabe, I. Sakai and Y. Mori, Serpentine acceleration in scaling FFAG, IPAC'11, (2011).

[39] E. Yamakawa, J-B. Lagrange, Y.Ishi, T. Ue- sugi, Y. Kuriyama, K.Okabe, I. Sakai and Y. Mori, Serpentine acceleration in scaling FFAG, IPAC'12, (2012).

[40] E. Yamakawa, T.Uesugi, J-B. Lagrange, Y. Kuriyama, Y.Ishi, and Y. Mori, Serpentine acceleration in zero-chromatic FFAG accelerators, Nucl. Instr. and Meth. A, to be published.

[41] E. Yamakawa, J.-B. Lagrange, T. Uesugi, Y. Kuriyama, Y. Ishi, Y. Mori, High intensity proton FFAG ring with serpentine acceleration for ADS, Proc. of HB 2012 2012.

[42] M. Fukuda, et al., Rev. Sci. Instrum. 74, 2293, (2003).

[43] S. Kurashima, Ph.D Thesis, Nagaoka University of Technology Dissertation.

[44] Th. Stammbach et al, The feasibility of high power cyclotrons, Nucl. Instr. and Meth. A, Vol. 113, p. 1-7 (1996).

[45] S. Adam et al., First operation of a flattop accelerating system in an isochronous cyclotron, IEEE Trans. NS 28(3) (1981) 2721

[46] M. Kanazawa, et al., Acceleration test with mixed higher harmonics in HIMAC, Proceedings of the 1st Annual Meeting of Particle Accelerator Society of Japan and the 29th Linear Accelerator Meeting in Japan, p.438-440. (2004).

[47] E. Miyazaki, et al., Fundamentals & applications of surface science, p. 834-837 (1991).

[48] W. R. Leo, Techniques for Nuclear and Particle Physics Experiment, Springer Verlag (1993).

[49] E. D. Courant, H. S. Snyder, Theory of the alternating-gradient synchrotron, Annals of Physics, Vol. 3 (1), p. 1-48 (1958).

[50] J.-B Lagrange, Study of zero-chromaticity in FFAG accelerators, Ph.D Thesis, Graduate School of Engineering, Kyoto University (2012).

[51] M. Nakajima, Technology of microwave, (1991).

[52] R. Bailey, RF for accelerators, Proc. of the CAS-CERN Accelerator School, p15-65, (2010).

[53] K. Takada, OHO '97, (1997)

[54] K. Oide, KEK, p. 195 (1992).

[55] J. M. Thijssen, COMPUTATIONAL PHYSICS, Springer, 2003.11 (2003).

List of reviewed publications

Related to the Chapter 2

Reviewed paper: T. Planche, E. Yamakawa, T. Uesugi, J.-B. Lagrange, Y. Kuriyama, K. Okabe, Y. Ishi and Y. Mori, Scaling FFAG rings for rapid acceleration of muon beams, Nuclear Instruments and Methods in Physics Research Section A, vol 622, Number 1, p. 21-27, 2010.

Related to the Chapter 3

Reviewed paper: E. Yamakawa , T.Uesugi and Y.Mori, Stationary Bucket Acceleration in the Scaling FFAG Accelerator, International Journal of Modern Physics A, Vol.26, Numbers 10-11, p. 1685-1872, 2011.

Reviewed paper: E. Yamakawa , T.Uesugi, J.-B. Lagrange, Y. Kuriyama, Y. Ishi and Y.Mori, Serpentine acceleration in zero-chromatic FFAG accelerators, Nuclear Instrument and Method in Physics Research Section A, submitted.

Conference proceeding: E. Yamakawa, T. Planche, J.-B Lagrange, T. Uesugi, Y. Kuriyama, Y. Ishi, Y. Mori, I. Sakai, K. Okabe and M. Inoue, THE STUDY OF NEW TYPE OF RF ACCELERATION IN SCALING FFAG ACCELERATION, 7th Annual Meeting of Particle Accelerator Society of Japan, p. 450-452, 2010.

Conference proceeding: E. Yamakawa, J-B. Lagrange, R. Nakano, Y.Ishi, T. Uesugi, Y. Kuriyama, B. Qin, K.Okabe, I. Sakai and Y. Mori, Serpentine acceleration in scaling FFAG, IPAC11, 2011.

Conference proceeding: E. Yamakawa, J-B. Lagrange, Y.Ishi, T. Uesugi, Y. Kuriyama, K.Okabe, I. Sakai and Y. Mori, Serpentine acceleration in scaling FFAG, IPAC12 conference proceedings, 2012.

Conference proceeding: E. Yamakawa, J.-B. Lagrange, T. Uesugi, Y. Kuriyama, Y. Ishi and Y. Mori, High intensity proton FFAG ring with serpentine acceleration for ADS, Proc. of HB 2012, 2012.

Related to the Chapter 4

Reviewed paper: E. Yamakawa , T.Uesugi, J.-B. Lagrange, Y. Kuriyama, Y. Ishi and Y.Mori, Serpentine acceleration in zero-chromatic FFAG accelerators, Nuclear Instrument and Method in Physics Research Section A, submitted.